Redox-active ligand-mediated assembly for high-performance transition metal oxide nanoparticle-based pseudocapacitors

Jeongyeon Ahn[a,1], Yongkwon Song[a,1], Ye Ji Kim[b], Donghyeon Nam[a], Taewoo Kim[b], Kyungwon Kwak[b], Cheong Hoon Kwon[c], Yongmin Ko[d,*], Suk Joong Lee[b,*], Jinhan Cho[a,e,*]

[a] *Department of Chemical and Biological Engineering, Korea University, 145 Anam-ro, Seongbuk-gu, Seoul 02841, Republic of Korea*

[b] *Department of Chemistry, Korea University, 145 Anam-ro, Seongbuk-gu, Seoul 02841, Republic of Korea*

[c] *Division of Energy Engineering, Kangwon National University, 346 Jungang-ro, Samcheok, 25913, Republic of Korea*

[d] *Division of Energy Technology, Materials Research Institute, Daegu Gyeongbuk Institute of Science and Technology (DGIST), 333 Techno Jungang-daero, Hyeonpung-eup, Dalseong-gun, Daegu 42988, Republic of Korea*

[e] *KU-KIST Graduate School of Converging Science and Technology, Korea University, 145 Anam-ro, Seongbuk-gu, Seoul 02841, Republic of Korea*

*Corresponding authors.
 E-mail addresses: yongmin.ko@dgist.ac.kr (Y. Ko), slee1@korea.ac.kr (S. J. Lee), jinhan71@korea.ac.kr (J. Cho)
[1]These authors contributed equally to this work.

Experimental Section

Materials

All chemical reagents for experiments were purchased from Sigma-Aldrich, and used without further purification. For the synthesis of MnPP, 2,6-dietoxybenzaldehyde and ethyl-4-formylbenzoate were synthesized according to the modified literature procedures [S1]. Organic solvents (ethanol, acetone, and toluene) were obtained from Daejung Chemicals & Metals (Republic of Korea).

Synthesis of OA-Fe$_3$O$_4$ NPs

OA-Fe$_3$O$_4$ NPs were prepared as previously reported [S2]. Iron(III) acetylacetonate (2 mmol), 1,2-hexadecanediol (10 mmol), OA (6 mmol), OAm (6 mmol), and benzyl ether (20 mL) were first mixed in a three-neck flask under inert gas condition. The reaction mixture was heated at 200 °C for 2 h, and then heated at 300 °C for 1 h. After the reaction was completed and cooled down to room temperature, the OA-Fe$_3$O$_4$ NPs mixture was purified by adding excess ethanol, and sequentially centrifuging in 8000 rpm for 10 min. The precipitated OA-Fe$_3$O$_4$ NPs were redissolved in toluene with OA (0.05 mL) and OAm (0.05 mL). Several centrifugation processes with excess ethanol were repeated, and final OA- Fe$_3$O$_4$ NPs in toluene was obtained.

Synthesis of OAm-ITO NPs

OAm-ITO NPs were prepared following the previous report [S3]. Indium(III) acetate (6.48 mmol), tin(II) ethylhexanoate (0.72 mmol), OAm (60 mmol), octanoic acid (21.6 mmol), and dicotyl ether (60 mL) were mixed in a three-neck flask, and heated at 80 °C for 1 h under vacuum. Then, the reaction mixture was heated at 150 °C for 1 h, and sequentially heated at 280 °C for 2 h under inert gas condition. After the reaction was completed and cooled down to room temperature, the OAm-ITO NPs mixture was purified by centrifugation with excess

acetone in 8000 rpm for 10 min. Several centrifugation processes with excess acetone were repeated, and the resultant OAm-ITO NPs in toluene was obtained.

Synthesis of MnPP

In the synthesis of MnPP, all of the reactions and manipulations of porphyrin building blocks were carried out under N_2 gas with the use of standard inert-atmosphere and Schlenk techniques unless otherwise noted. Solvent used in inert-atmosphere reactions were dried and degassed using standard procedures. Flash column chromatography was carried out with 230-400 mesh silica gel from Sigma-Aldrich using wet-packing method.

Scheme S1. Synthesis of Mn(III)-porphyrin.
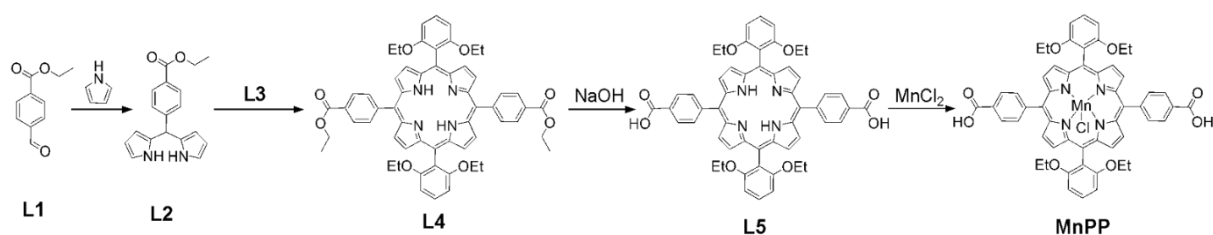
Ethyl-4-formylbenzoate (L1). 4-formylbenzoicacid (10 g, 66.6 mmol) was dissolved in freshly distilled AcCN and degassed with N_2 gas for 15 min. Then, K_2CO_3 (11 g, 79.6 mmol) and bromoethane (10.9 g, 100.0 mmol) were added and the resulting mixture was refluxed overnight under N_2 gas. The mixture was diluted with ethyl acetate and quenched with 0.1 M NaOH. After washing with water, the organic was dried over anhydrous sodium sulfate. After filtration, the organic was evaporated to dryness using a rotary evaporator. The residue was purified by silica-gel column chromatography (ethyl acetate/hexane 1:4 v/v) to afford pure **L1** as a white solid (6.5 g, 54.0 %). ^{1}H NMR (CDCl$_3$): δ 10.1 (s, 1H), 8.20 (d, $^3J_{\text{H-H}}$ = 8.79 Hz, 2H), 7.95 (d, $^3J_{\text{H-H}}$ = 8.24 Hz, 2H), 4.41 (q, $^3J_{\text{H-H}}$ = 7.1 Hz, 2H), 1.14 (t, $^3J_{\text{H-H}}$ = 7.14 Hz, 3H).

***meso*-(4-Carboxyethylphenyl)dipyrromethane (L2)**. **L1** (5 g, 28.06 mmol) was dissolved in freshly distilled pyrrole (52.5 ml, 756.70 mmol) in a 100 mL round-bottom flask equipped with a magnetic stirring. The mixture was degassed for 10 min and trifluoroacetic acid (TFA, 0.25

ml, 3.30 mmol) was injected into the reaction solution via syringe. The resulting mixture was stirred for 20 min under N_2 gas. After quenching with aqueous sat. NaOH solution (0.1 M), ethyl acetate was added. The mixture was washed with water (2 × 50 mL), dried over anhydrous $MgSO_4$, and concentrated to dryness using a rotary evaporator. The resulting oily residue was purified by silica-gel column chromatography (ethyl acetate/dichloromethane 0.2:9.8 v/v) to afford pure **L2** as a white solid (5.2 g, 61.5 %). ^{1}H NMR (CDCl$_3$): δ 7.96 (d, $^3J_{H-H}$ = 7.8 Hz, 2H), 7.26 (d, $^3J_{H-H}$ = 7.8 Hz, 2H), 6.69 (dd, $^3J_{H-H}$ = 1.6 Hz, 2H), 6.15 (dd, $^3J_{H-H}$ = 3.1 Hz, 2H), 5.89 (bs, 2H), 5.56 (s, 1H), 4.35 (q, $^3J_{H-H}$ = 7.04 Hz, 2H), 1.37 (t, $^3J_{H-H}$ = 7.04 Hz, 3H), ^{13}C NMR (CDCl$_3$) : δ 166.66, 147.43, 131.85, 130.10, 129.40, 128.61, 117.78, 108.77, 107.73, 61.20, 44.17, 14.58.

2,6-Diethoxybenzaldehyde (L3). *N,N,N′,N′*-Tetramethylethylenediamine (TMEDA, 7.1 mL, 47.66 mmol) and diethoxybenzene (10 g, 60.16 mmol) in distilled diethylether was added *n*-BuLi (2.5 M in hexane, 26.13 mL, 65.30 mmol) at 0 ºC over a period of 30 min. The reaction mixture was stirred for 3 h under N_2 gas. After warming up to room temperature, *N,N*-dimethylformamide (DMF, 8.85 mL, 114.30 mmol) was added dropwise, and the resulting mixture was stirred for an additional 2 h. After quenching with water, the mixture was extracted with ethyl acetate 4-times, the organic was combined and evaporated to dryness using a rotary evaporator to yield a yellow residue, which was purified by silica-gel column chromatography (ethyl acetate/hex 1:5 v/v) to afford pure **L3** as a white solid (9.1 g, 77.7 %). ^{1}H NMR (CDCl$_3$): δ 10.5 (s, 1H), 7.39 (t, $^3J_{H-H}$ = 8.07 Hz, 1H), 6.54 (d, $^3J_{H-H}$ = 8.95 Hz, 2H), 4.11 (q, $^3J_{H-H}$ = 7 Hz, 4H), 1.46 (t, $^3J_{H-H}$ = 6.87Hz, 6H).

5,15-Bis(4-carboxyethylphenyl)-10,20-bis[2,6-diethoxyphenyl]porphyrin (L4). L2 (1 g, 3.4 mmol) and **L3** (0.66 g, 3.4 mmol) were dissolved in dichloromethane (600 mL) in a 1 L round-bottom flask equipped with a magnetic stirring. The mixture was degassed for 15 min and was then allowed to reflux for 4 h under N_2 gas. 2,3-Dichloro-5,6-dicyano-1,4-benzoquinone (DDQ, 1g) was added and refluxed for another 30 min. After cooling to room temperature, pyridine

(3.4 ml) was injected into the reaction mixture via syringe. Then, the resulting mixture was evaporated to dryness using a rotary evaporator to yield a dark residue, which was redissolved in dichloromethane. The solution was filtered and washed with dichloromethane. The resulting solution was evaporated to dryness using a rotary evaporator and the residue was purified by silica-gel column chromatography (100% dichloromethane). After recrystallization from the mixture of dichloromethane and methanol, a pure **L4** was obtained as a purple solid (248 mg, 15.6 %). ^{1}H NMR (CDCl$_3$): δ 8.82 (d, $^3J_{\text{H-H}}$ = 4.70 Hz, 4H), 8.72 (d, $^3J_{\text{H-H}}$ = 4.70 Hz, 4H), 8.42 (d, $^3J_{\text{H-H}}$ = 7.83 Hz, 4H), 8.32 (d, $^3J_{\text{H-H}}$ = 7.83 Hz, 4H), 7.68 (t, $^3J_{\text{H-H}}$ = 8.61 Hz 2H), 6.98 (d, $^3J_{\text{H-H}}$ = 8.61 Hz, 4H), 4.57 (q, $^3J_{\text{H-H}}$ = 7.04 Hz, 4H), 3.88 (q, $^3J_{\text{H-H}}$ = 7.04 Hz 8H), 1.55 (t, $^3J_{\text{H-H}}$ = 7.04 Hz 6H), 0.60 (t, $^3J_{\text{H-H}}$ = 7.04 Hz 12H). ^{13}C NMR (CDCl$_3$) : δ 167.22, 160.08, 147.57, 134.83, 130.26, 129.78, 127.94, 117.69, 113.41, 105.63, 77.44, 77.08, 76.77, 76.45, 64.44, 61.48, 14.75, 14,61, 1.27. MS (MALDI-TOF): m/z= 934.360 for M$^+$; Calcd 935.07.

5,15-Bis(4-carboxyphenyl)-10,20-bis[2,6-diethoxyphenyl]porphyrin (L5). L4 (200 mg, 0.21 mmol) in tetrahydrofuran (THF, 20 mL) was added to a 40 % aqueous solution of KOH (20 mL) and was degassed with N$_2$ gas for 10 min. The mixture was allowed to reflux for overnight. After cooling to room temperature, the resulting mixture was evaporated to dryness and the solid was redissolved in methanol, and 10 % HCl was added. After extracting the product with dichloromethane, the product was purified by silica-gel column chromatography (methanol/dichloromethane/triethylamine 9:1:0.01v/v/v) to afford pure **L5** as a purple solid (178 mg, 94.6 %). ^{1}H NMR (DMSO): δ 8.71 (m, 8H), 8.20 (d, $^3J_{\text{H-H}}$ = 7.04 Hz, 4H), 8.02 (d, $^3J_{\text{H-H}}$ = 7.04 Hz, 4H), 7.71 (t, $^3J_{\text{H-H}}$ = 8.61 Hz, 2H), 7.09 (d, $^3J_{\text{H-H}}$ = 7.83 Hz, 4H), 3.88 (q, $^3J_{\text{H-H}}$ = 7.04 Hz, 8H), 0.47 (t, $^3J_{\text{H-H}}$ = 7.04 Hz, 12H). ^{3}C NMR (DMSO): δ 168.38, 159.76, 139.87, 135.01, 128.53, 125.57, 119.73, 118.39, 113.87, 106.12, 67.68, 64.28, 55.59, 46.03, 31.08, 14.87, 10.21. MS (MALDI-TOF): m/z= 878.191 for M$^+$; Calcd 878.97.

{5,15-Bis(4-carboxyphenyl)-10,20-bis[2,6-diethoxyphenyl]porphyrinato}manganese(III) chloride (MnPP). A solution of **L5** (250 mg, 0.26 mmol) and MnCl$_2$·4H$_2$O (514 mg, 2.60

mmol) in *N,N*- dimethylformamide (DMF, 12.5 mL) was heated to reflux for 6 h. The reaction was monitored by UV-Vis spectrum. The reaction mixture was cooled to room temperature and then DMF was evaporated under reduced pressure. Then, the resulting residue was dispersed in water, filtered, and dried in vacuum. The crude product was purified by column chromatography (methanol/dichloromethane/triethylamine 1:6:0.01 v/v/v). After recrystallization from the mixture of dichloromethane and methanol, a pure MnPP was obtained as a dark green solid (227 mg, 82.5 %). MS (MALDI-TOF): *m/z*= 931.298 for [M-Cl]$^+$; Calcd 931.89.

LbL assembly of (Fe$_3$O$_4$ NP/ligand/ITO NP/ligand)$_m$ multilayers

The concentrations of NPs in toluene and ligands in ethanol were adjusted to 10 mg mL^{-1} (for OA-Fe$_3$O$_4$ NPs), 10 mg mL^{-1} (for OAm-ITO NPs), 0.3 mg mL^{-1} (for MnPP), and 0.1 mg mL^{-1} (for PAA). Substrates (including Si wafers, gold-sputtered Si wafers, quartz glasses, QCM electrodes, and FTO glasses) were cleaned using an UV−ozone cleaner for 30 min. Additionally, the Ni-electroplated TCCs were prepared following the previously reported literature [S4] and used without further surface treatment. Then, the substrates were dipped into NH$_2$-functionalized poly(ethyleneimine) (PEI) solution (1 mg mL^{-1} in ethanol) for 30 min as a buffer layer for the sequent deposition, and washed with pure ethanol to remove weakly adsorbed materials. The PEI-coated substrates were dipped into OA-Fe$_3$O$_4$ NP solution with washing by pure toluene, and sequentially dipped into ligand (MnPP or PAA) solution with washing by pure ethanol. In the same way, they were dipped into OAm-ITO NP solution (and washed) and into ligand solution (and washed), resulting in one periodic layer of (Fe$_3$O$_4$ NP/ligand/ITO NP/ligand)$_m$ multilayers. In this case, the dipping time was fixed to be 5 min each material. These procedures were repeated until the desired layer number was obtained.

Characterization

The size and crystalline structure of OA-Fe$_3$O$_4$ NPs and OAm-ITO NPs were examined

by HR-TEM (Tecnai F20, FEI). The structure of MnPP was examined by NMR spectra, recorded on a Varian AS400 (399.937 MHz for ^{1}H and 100.573 MHz for ^{13}C) spectrometer. ^{1}H chemical shifts are referenced to the proton resonance resulting from protic residue in deuterated solvent and ^{13}C chemical shift recorded downfield in ppm relative to the carbon resonance of the deuterated solvents. Matrix-Assisted Laser-Desorption-Ionization Time-of-flight Mass Spectra (MALDI-TOF) were obtained using a Bruker Daltonics LRF20 MALDI-TOF Mass Spectrometer. FTIR analysis of pristine materials and multilayers on gold-sputtered Si wafers were carried out using a Cary 600 (Agilent Technologies) in an advanced grazing angle (AGA) specular mode that can detect the mono-molecule of the outermost layer, followed by smoothing and baseline correction using spectral analysis software (OMNIC, Thermo Fisher Scientific). The growth analysis of multilayers on quartz glasses was examined by using UV−vis spectroscopy (Lambda 365, Perkin Elmer) in a wavelength ranging from 200 to 800 nm. The mass change (Δm, μg cm^{-2}) of multilayers was calculated from the frequency change ($-\Delta F$, Hz) monitored by QCM 200 (SRS) using the Sauerbrey equation [S5]. FE-SEM and EDS elemental mapping images were obtained using a S-4800 (Hitachi). The mass ratio of Mn and Fe in the multilayer was measured by ICP-MS using an Elan DRCII (Perkin Elemer). By considering the total mass and stoichiometry of the multilayers, the mass loading of each component was calculated.

DFT Calculation

All density functional theory (DFT) calculations were performed using the Gaussian 0 9 program package in gas phase. For Mn(III)-porphyrin-Cl complex, the basis set chosen for t he C, H, O, N and Cl ion was 6-31G(d,p). The nonrelativistic Hartree-Fock effective core potential method and the corresponding basis sets (LANL2DZ) were used for the Mn ion. The complexes were energetically optimized by Becke 3-parameter exchange and Lee-Yang-Parr c orrelation functionals (B3LYP).

Electrochemical Measurements

CV, GCD, and EIS measurements of electrodes were evaluated in a three-electrode system using an Ivium-n-Stat workstation (Ivium Technologies) at room temperature. Ag/AgCl (saturated in 3M NaCl aqueous solution) electrodes and Pt wires (or Pt meshes) were used as the reference electrodes and counter electrodes, respectively. The electrochemical measurements of electrodes on flat FTO glasses and on TCCs were conducted in aqueous Na_2SO_3 electrolyte with a concentration of 0.5 and 1.0 mol L^{-1}, respectively, of which different concentrations were used due to the large difference in active surface area. CV/GCD measurements and EIS measurements were carried out in the potential window from −0.9 to 0 V (*vs.* Ag/AgCl) and in the frequency ranging from 10^5 to 0.1 Hz, respectively. The areal/specific/volumetric capacitance values were calculated from the GCD curves based on the active area (C_{areal}), total mass ($C_{specific}$) and film thickness (C_{vol}) of electrodes.
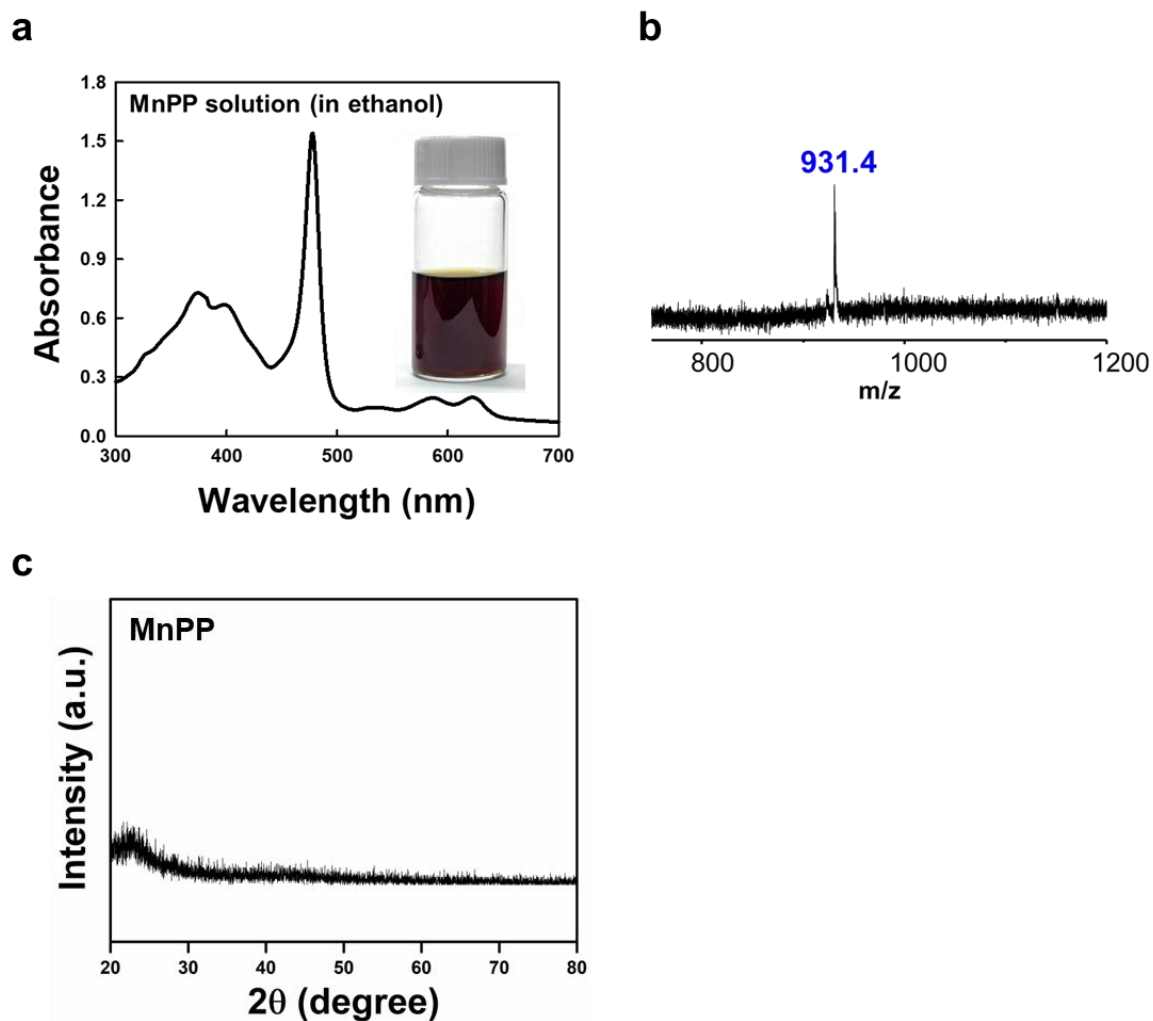
Fig. S1. Material characterization of {5,15-Bis(4-carboxyphenyl)-10,20-bis[2,6-diethoxy phenyl]porphyrinato}manganese(III) chloride (MnPP). (a) UV−vis spectrum and photograph (inset) of MnPP solution (in ethanol). The absorbance peaks for Soret band (at 478 nm) and Q band (at 580−620 nm) originated from the macrocycle ring of MnPP. (b) MALDI-TOF and (c) XRD pattern of MnPP.
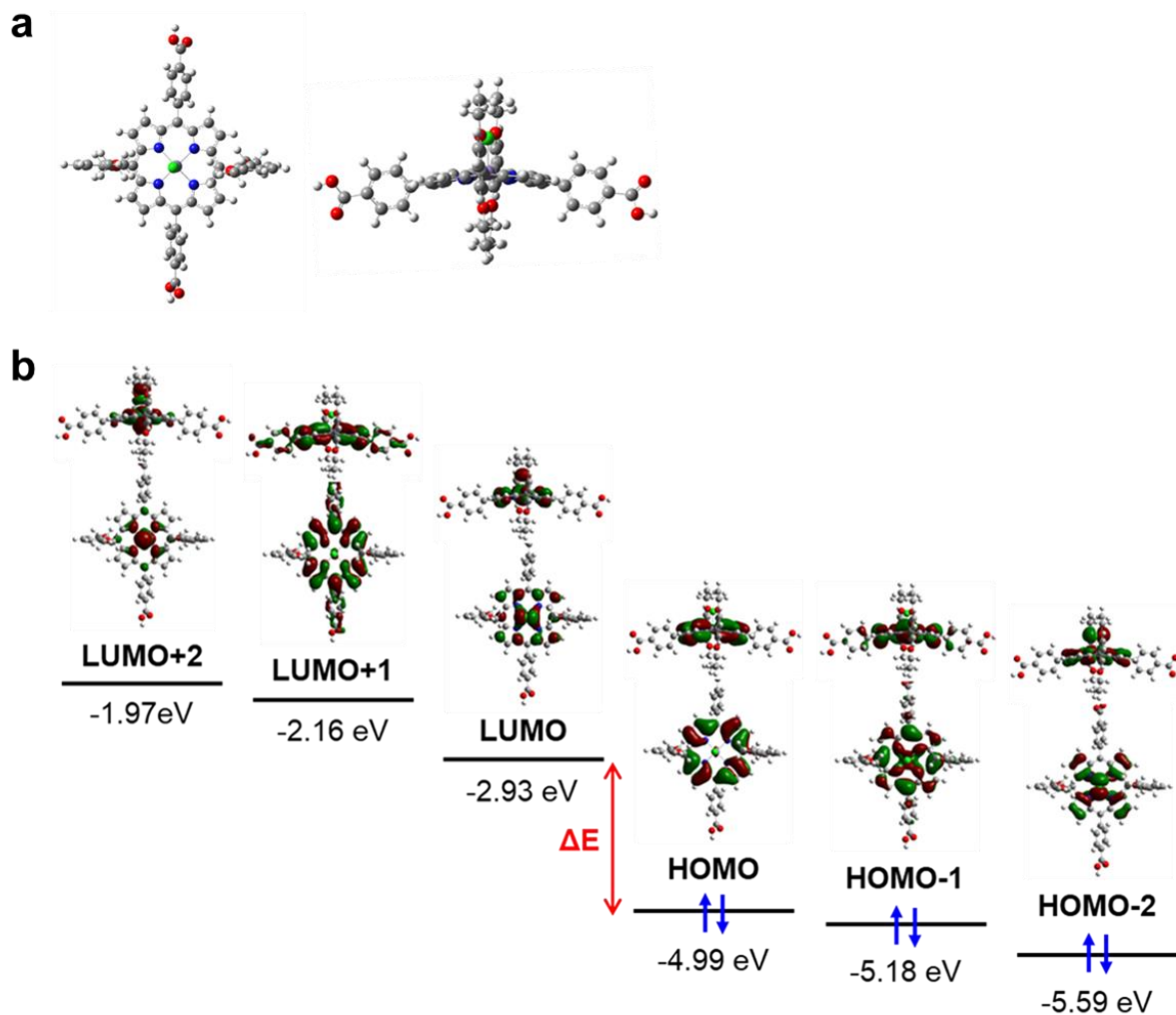
Fig. S2. DFT calculation of MnPP molecules. (a) Optimized molecular structures of neutral MnPP. (b) Electron configuration and corresponding frontier orbital diagram of neutral MnPP molecules. The energy gap between HOMO and LUMO (ΔE) was calculated to be ~2.06 eV.
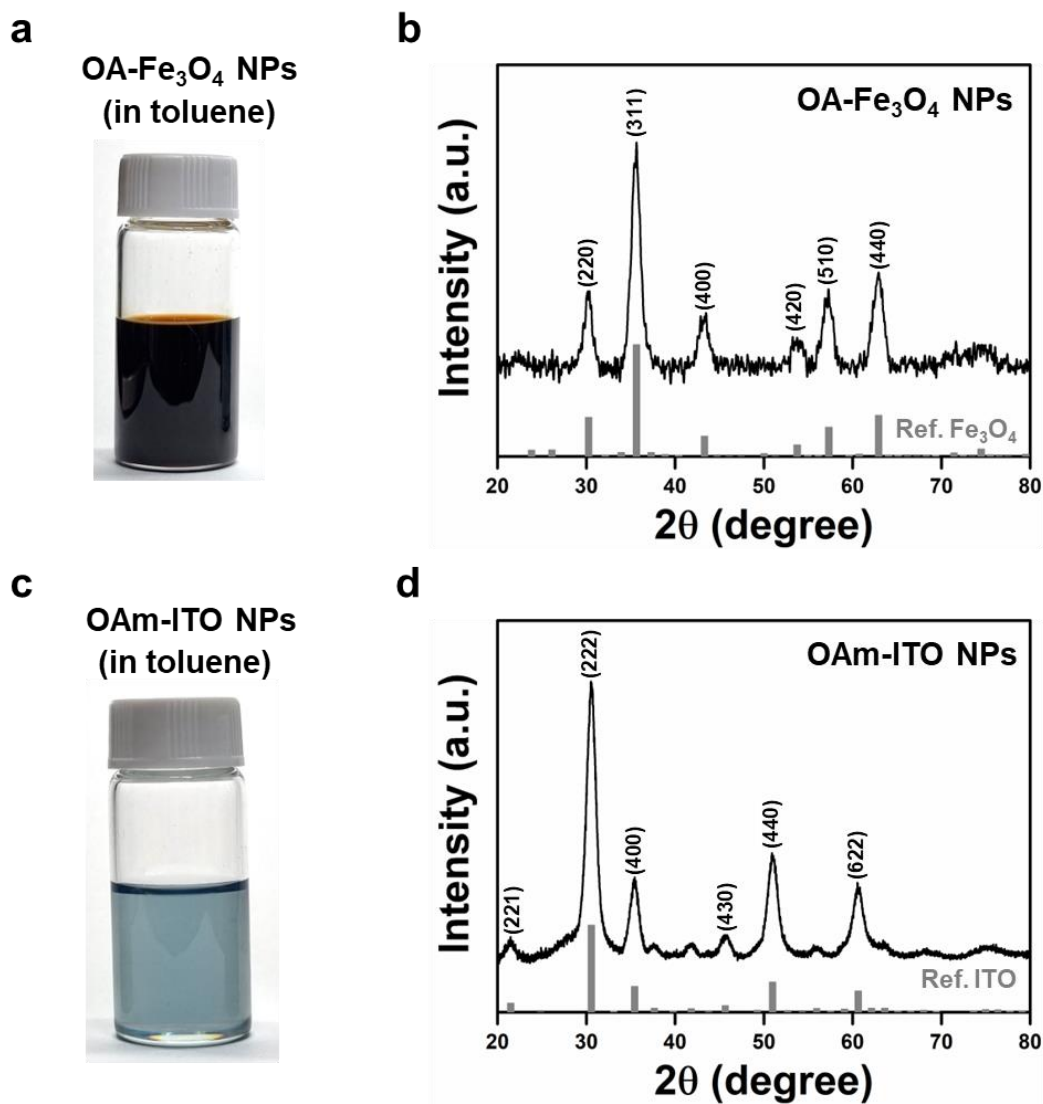
Fig. S3. (a) Photograph of OA-Fe$_3$O$_4$ NPs solution in toluene and (b) XRD pattern of OA-Fe$_3$O$_4$ NPs (top) with referential Fe$_3$O$_4$ (bottom) (JCPDS card No. 65-3107) (c) Photograph of OAm-ITO NPs solution in toluene and (d) XRD pattern of OAm-ITO NPs (top) with referential ITO (bottom) (JCPDS card No. 06-0416).
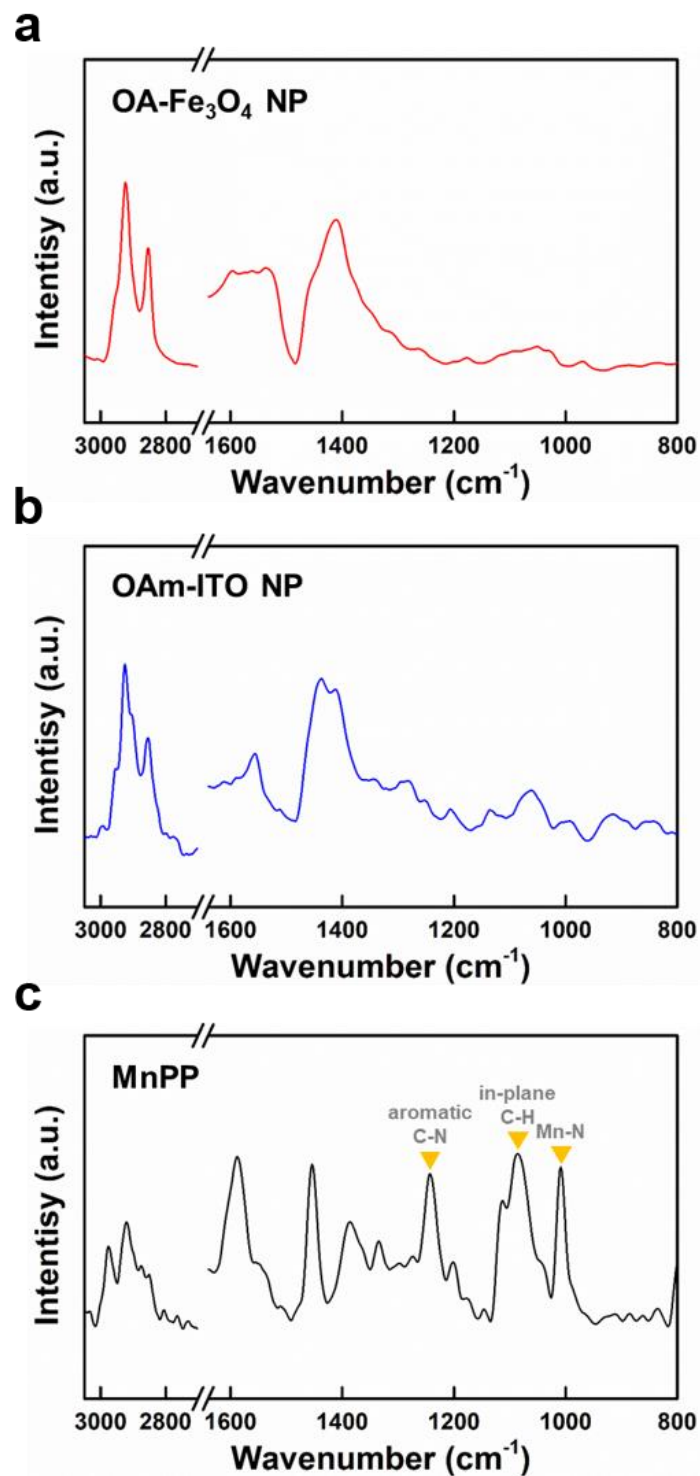
Fig. S4. FTIR spectra of pristine (a) OA-Fe$_3$O$_4$ NP, (b) OAm-ITO NP, and (c) MnPP. The absorption peaks of MnPP originated from aromatic C-N (at 1244 cm^{-1}), in-plane C-H (at 1086 cm^{-1}), and Mn-N (at 1011 cm^{-1}) vibrations, which did not overlap with those of OA-Fe$_3$O$_4$ NP and OAm-ITO NP in the same wavenumber region [S6].
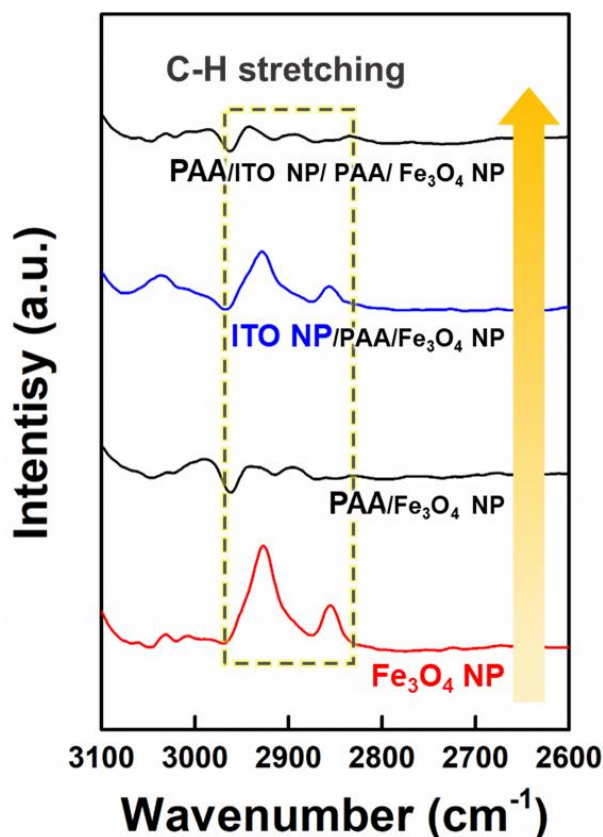
Fig. S5. FTIR spectra of $(Fe_3O_4$ NP/PAA/ITO NP/PAA)$_m$ multilayers obtained by sequentially depositing each layer. The pristine OA-Fe_3O_4 NPs and OAm-ITO NPs displayed the obvious C-H stretching peaks originating from the long aliphatic chains of native OA/OAm ligands at 2924 and 2854 cm^{-1}, where the PAA exhibited almost no distinct absorption peaks. Therefore, the presence of residual native OA/OAm ligands within the multilayers could be detected by monitoring the C-H stretching peaks. Specifically, when the PAA was assembled onto the OA-Fe_3O_4 NP-coated substrate (see the PAA/Fe_3O_4 NP), the intensity of C-H stretching peaks was significantly decreased, indicating that the native OA ligands bound to the surface of Fe_3O_4 NPs were successfully replaced with the multiple COOH groups of PAA. Sequentially, when OAm-ITO NPs were deposited onto the PAA/Fe_3O_4 NP/substrate (see the ITO NP/PAA/Fe_3O_4 NP), the absorption peak intentisy of native OAm ligands was notably increased again. That is, the alternating depositions of OA-Fe_3O_4 NPs (or OAm-ITO NPs) and PAA resulted in the repetition

13

of the appearance and disappearance of C-H stretching peaks, implying the consecutive ligand

exchange reaction between the native OA/OAm ligands and the multiple COOH groups of PAA

on the surface of oxide NPs.
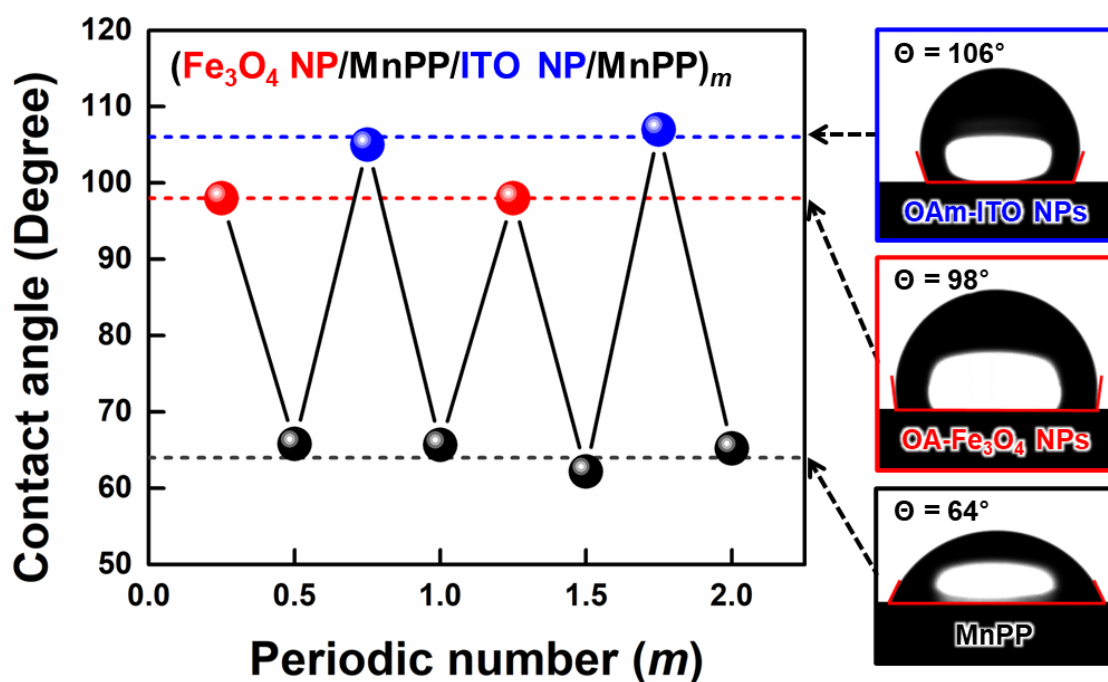
Fig. S6. The periodic change of water contact angles of (Fe$_3$O$_4$ NP/MnPP/ITO NP/MnPP)$_m$ multilayers according to the type of the outermost layer. The average contact angles were measured to be ~106° for the outermost OAm-ITO NPs layer, ~98° for the outermost OA-Fe3O4 NPs layer, and ~64° for the outermost MnPP layer.
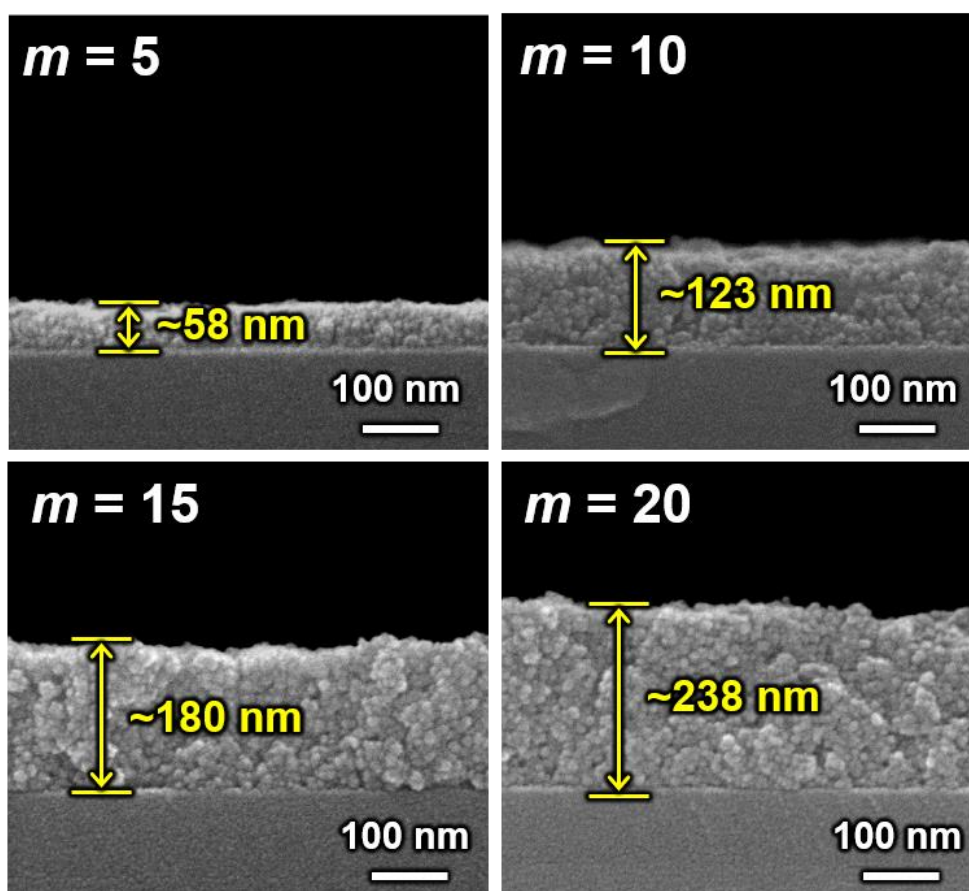
Fig. S7. Cross-sectional FE-SEM images and total film thicknesses of (Fe_3O_4 NP/MnPP/ITO NP/MnPP)$_m$ multilayers with increasing the periodic number (*m*) from 5 to 20.

a

	Mn	Fe
mass (mg)	0.0002	0.017

b

	MnPP	Fe_3O_4 NP	ITO NP	Total film
mass (mg)	0.0034	0.024	0.0426	0.07
mass fraction (%)	4.9	34.3	60.8	100

Fig. S8. (a) ICP-MS data for (Fe_3O_4 NP/MnPP/ITO NP/MnPP)$_m$ multilayers and (b) the corresponding mass/mass fraction of each component.
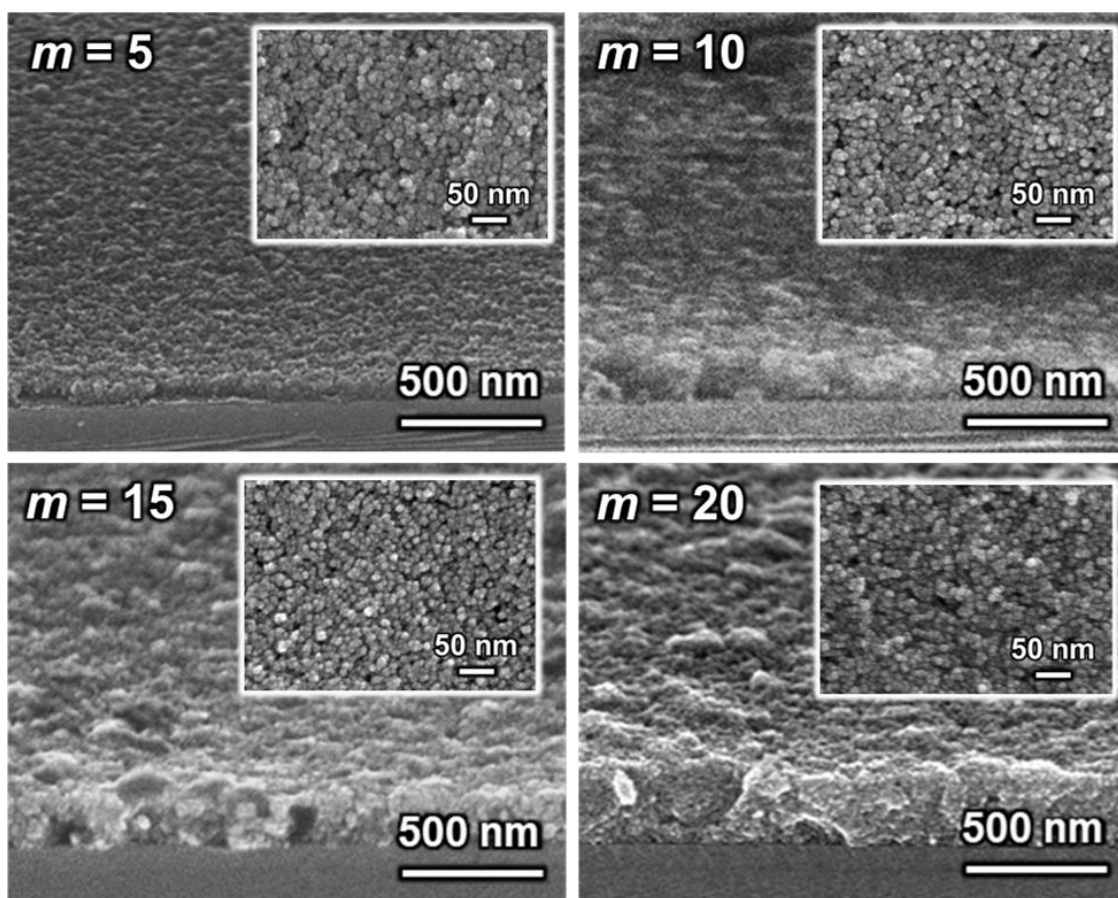
Fig. S9. Tilted and planar (the insets) FE-SEM images of (Fe_3O_4 NP/MnPP/ITO NP/MnPP)$_m$ multilayers with increasing the periodic number (m) from 5 to 20.
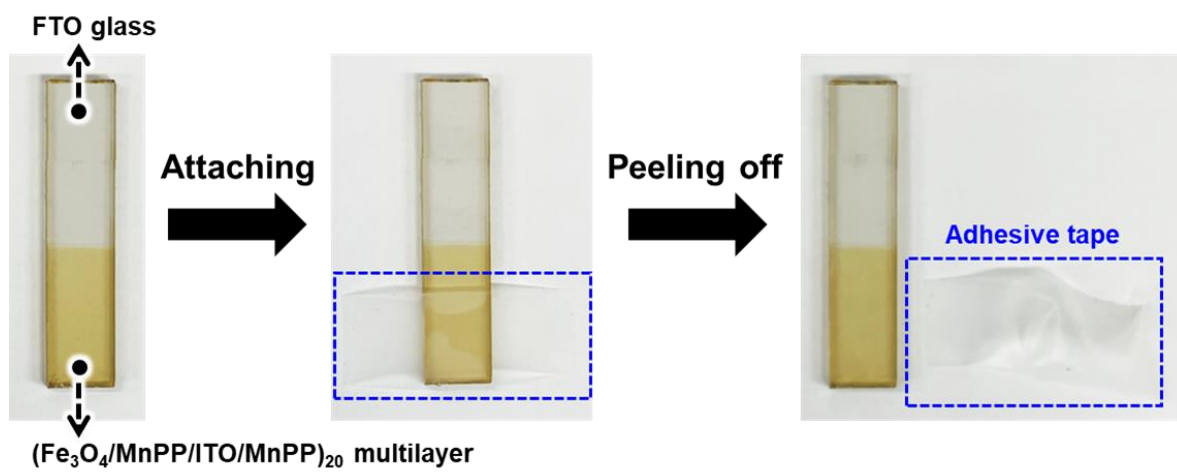
Fig. S10. Peeling test of $(Fe_3O_4 \text{ NP/MnPP/ITO NP/MnPP})_{20}$ electrode with a 3M adhesive tape.
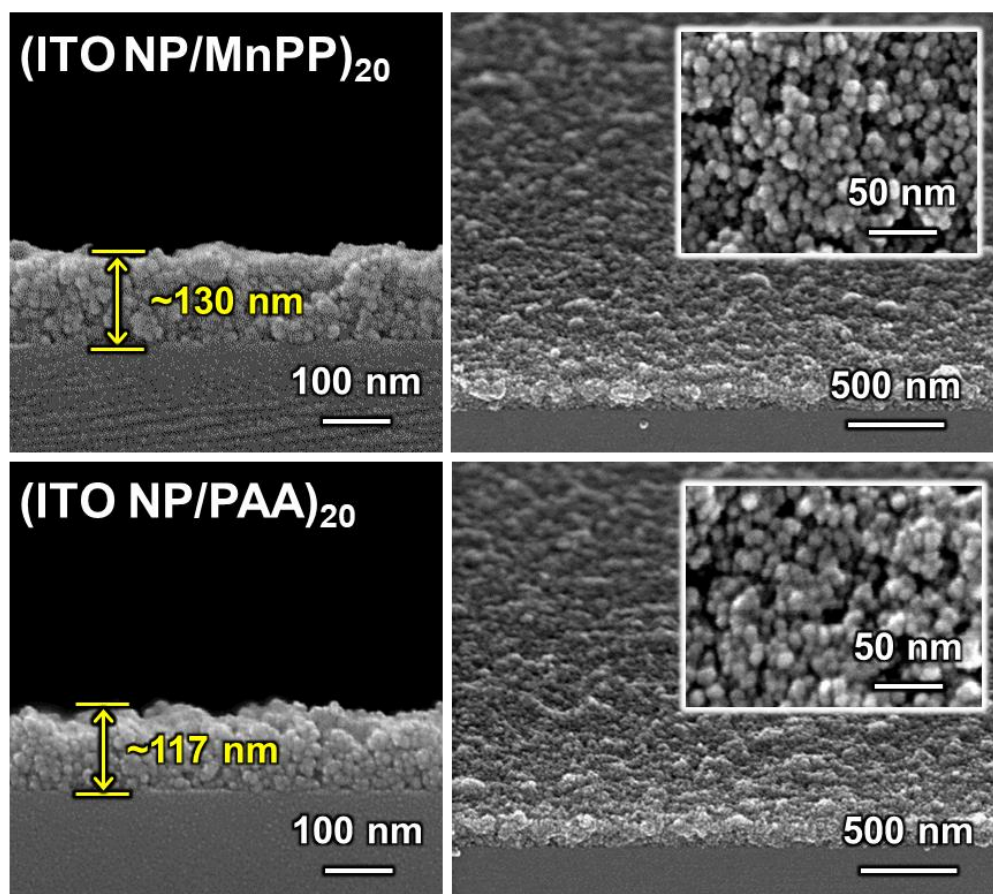
Fig. S11. Cross-sectional (left panels), tilted (right panels), and planar (the insets of right panels) FE-SEM images of (ITO NP/MnPP)$_{20}$ and (ITO NP/PAA)$_{20}$ multilayers.
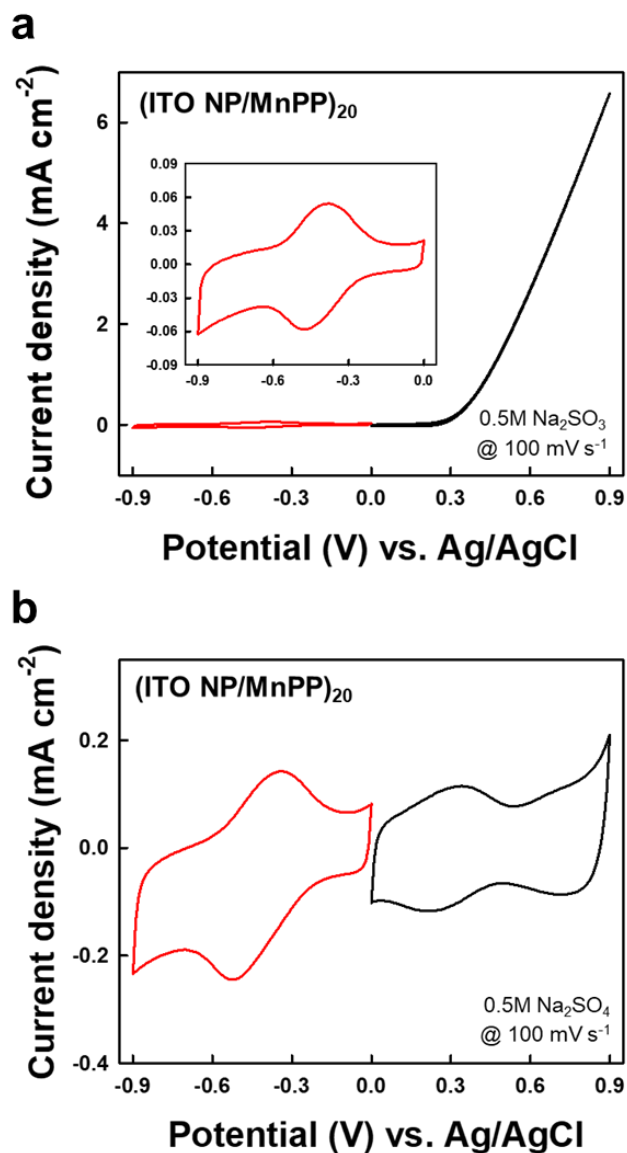
Fig. S12. CV curves of (ITO NP/MnPP)$_{20}$ electrode at a scan rate of 100 mV s^{-1} using aqueous (a) Na$_2$SO$_3$ and (b) Na$_2$SO$_4$ electrolytes in the potential windows ranging from −0.9 to 0 V and from 0 to 0.9 V (*vs.* Ag/AgCl). In the case of using a Na$_2$SO$_3$ electrolyte, the irreversible oxidation of sulfite anions (SO$_3^{2-}$) started at the potential over ~0.2 V [S7], which limited the stable electrochemical operation in negative potential range. When using a Na$_2$SO$_4$ electrolyte, it was found that the (ITO NP/MnPP)$_{20}$ electrode exhibited two prominent redox pairs (i.e., one (−0.52/−0.34 V) in the negative potential range of −0.9 to 0 V and the other (0.22/0.33 V) in the positive potential range of 0 to 0.9 V).
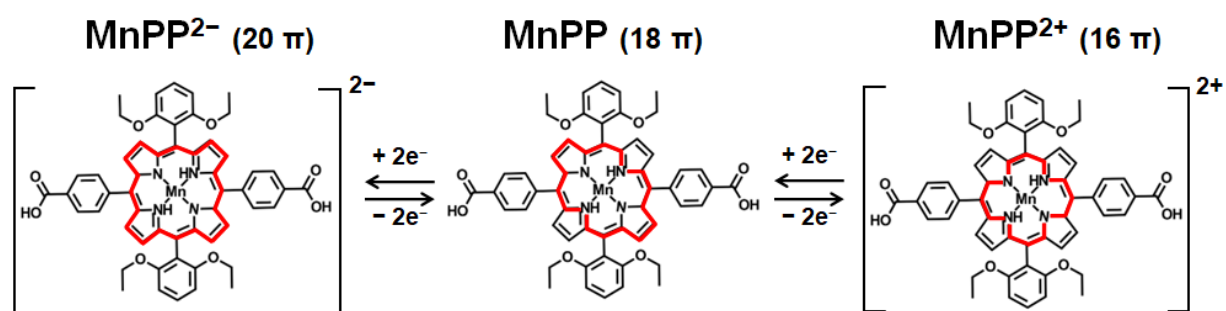
Fig. S13. Redox mechanism of MnPP molecules mediated by two conjugated π electrons. The red bold line on the porphyrin ring indicates π-conjugation circuit.
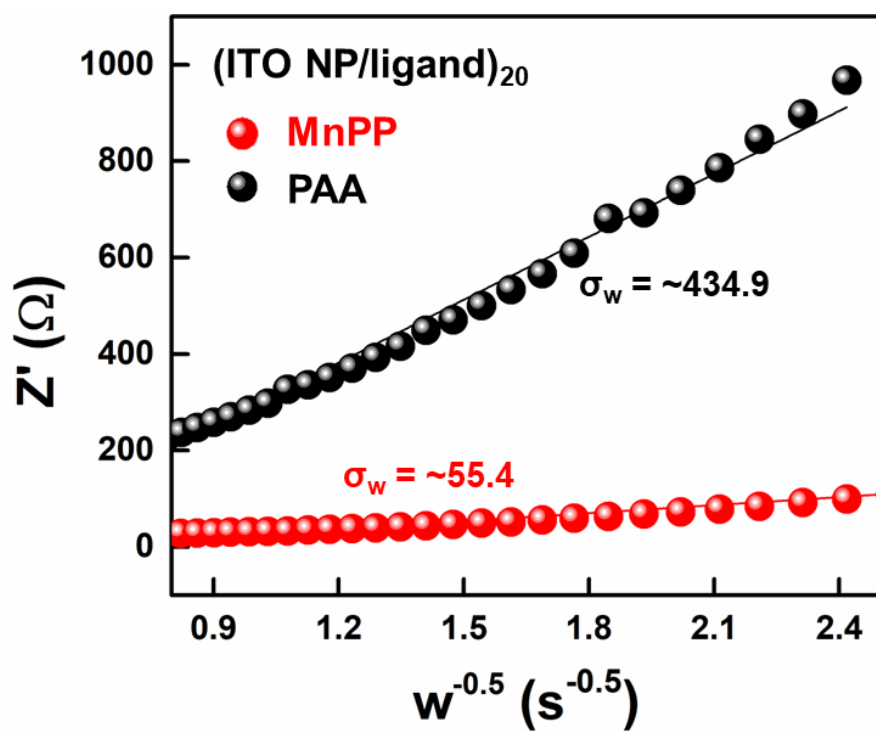
Fig. S14. Warburg impedance coefficient (σ_w) plots with fitted lines of (ITO NP/MnPP)$_{20}$ and (ITO NP/PAA)$_{20}$ electrodes.
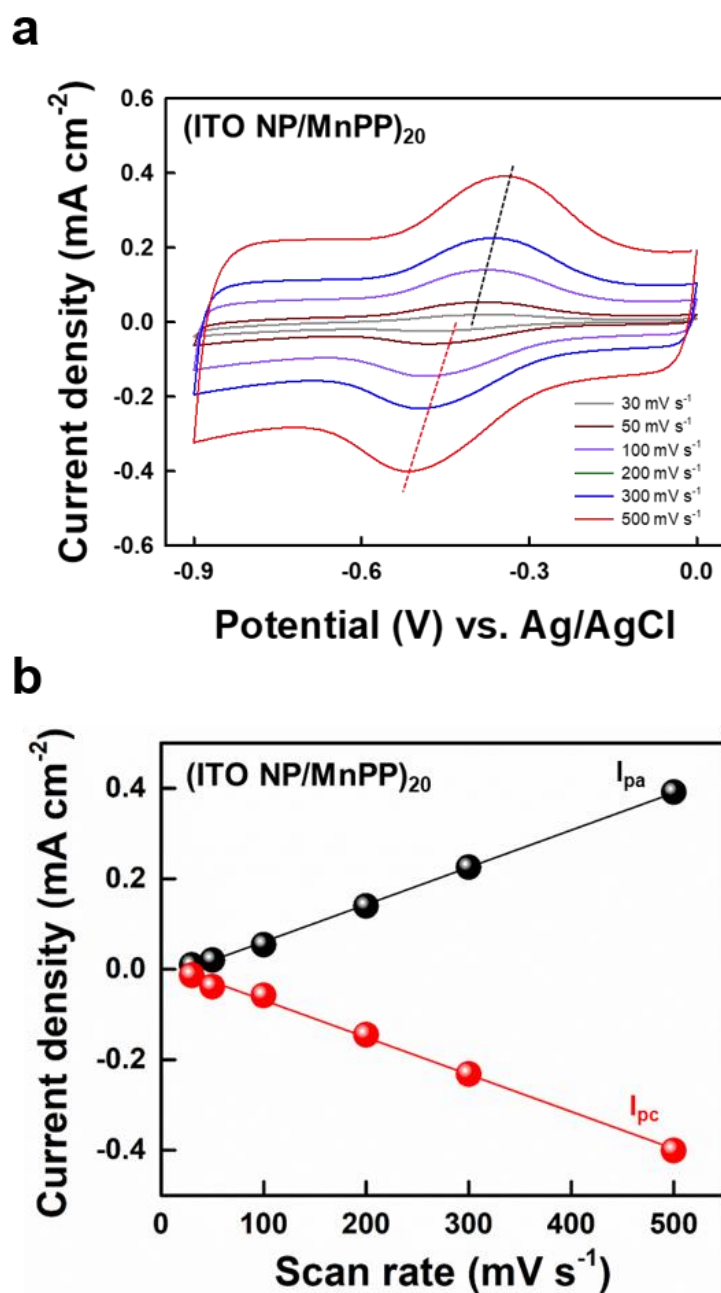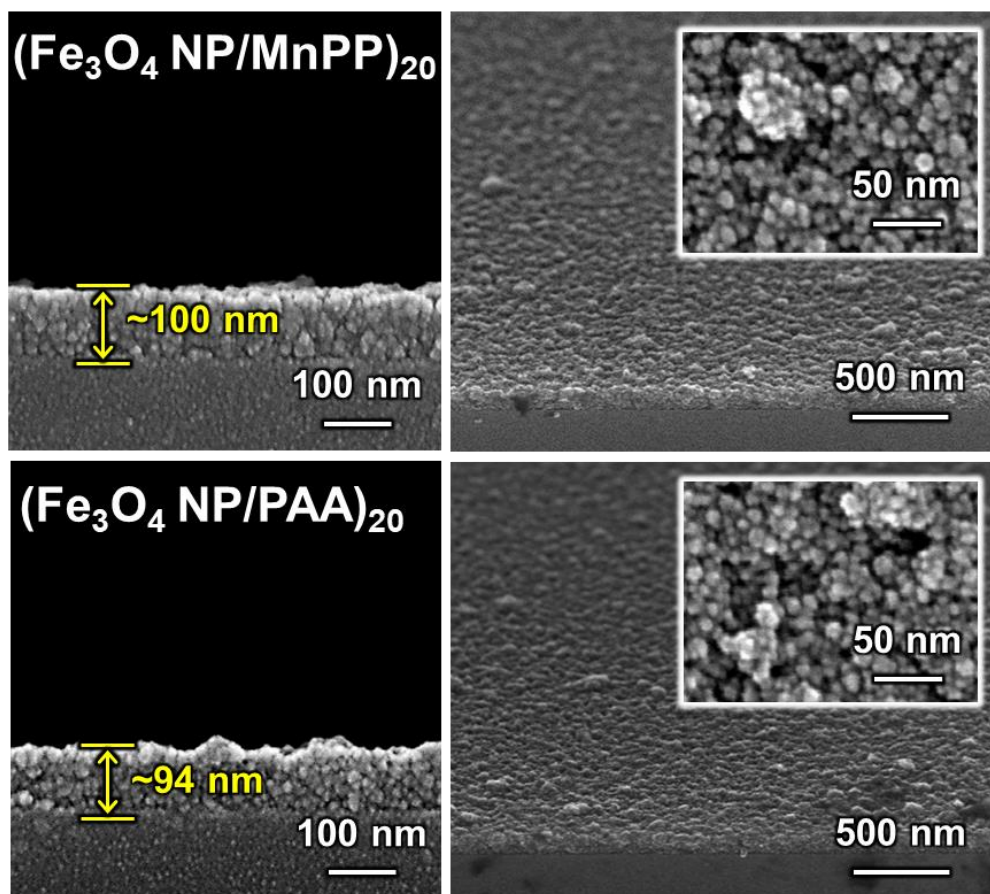
Fig. S15. **(**a) CV curves of (ITO NP/MnPP)$_{20}$ electrode with increasing the scan rate from 30 to 500 mV s^{-1} and corresponding (b) anodic (black circles and line) and cathodic (red circles and line) peak current densities as a function of scan rate.

Fig. S16. Cross-sectional (left panels), tilted (right panels), and planar (the insets of right panels) FE-SEM images of (Fe$_3$O$_4$ NP/MnPP)$_{20}$ and (Fe$_3$O$_4$ NP/PAA)$_{20}$ multilayers.
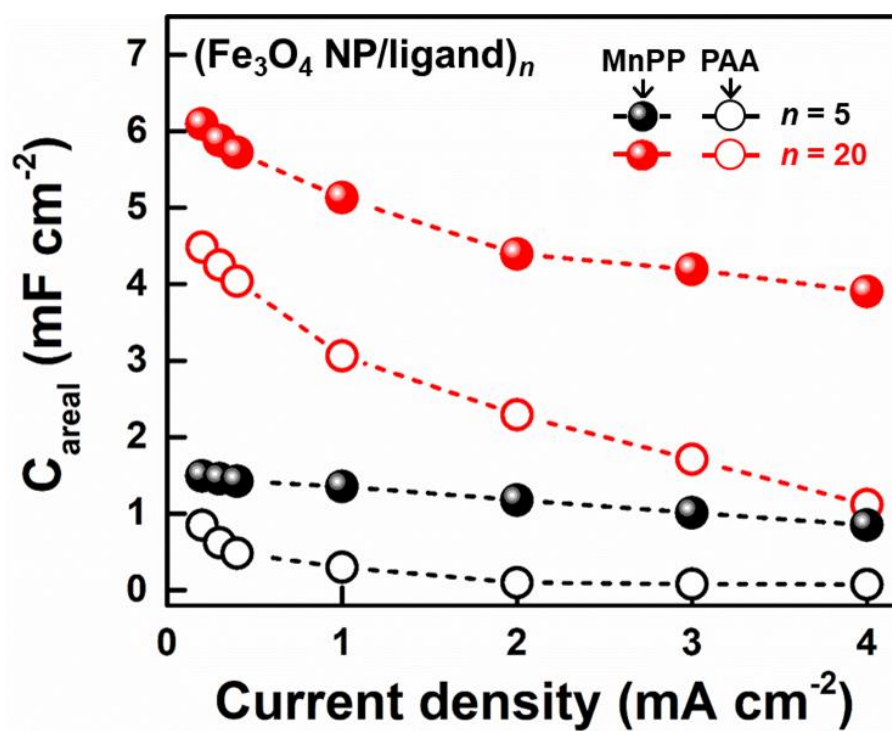
Fig. S17. Areal capacitance (C_{areal}) of $(Fe_3O_4$ NP/ligand)$_n$ with increasing the current density from 0.2 to 4.0 mA cm^{-2} at the bilayer number of 5 and 20. The MnPP and PAA ligands are represented as closed circles (MnPP) and open circles (PAA), respectively.
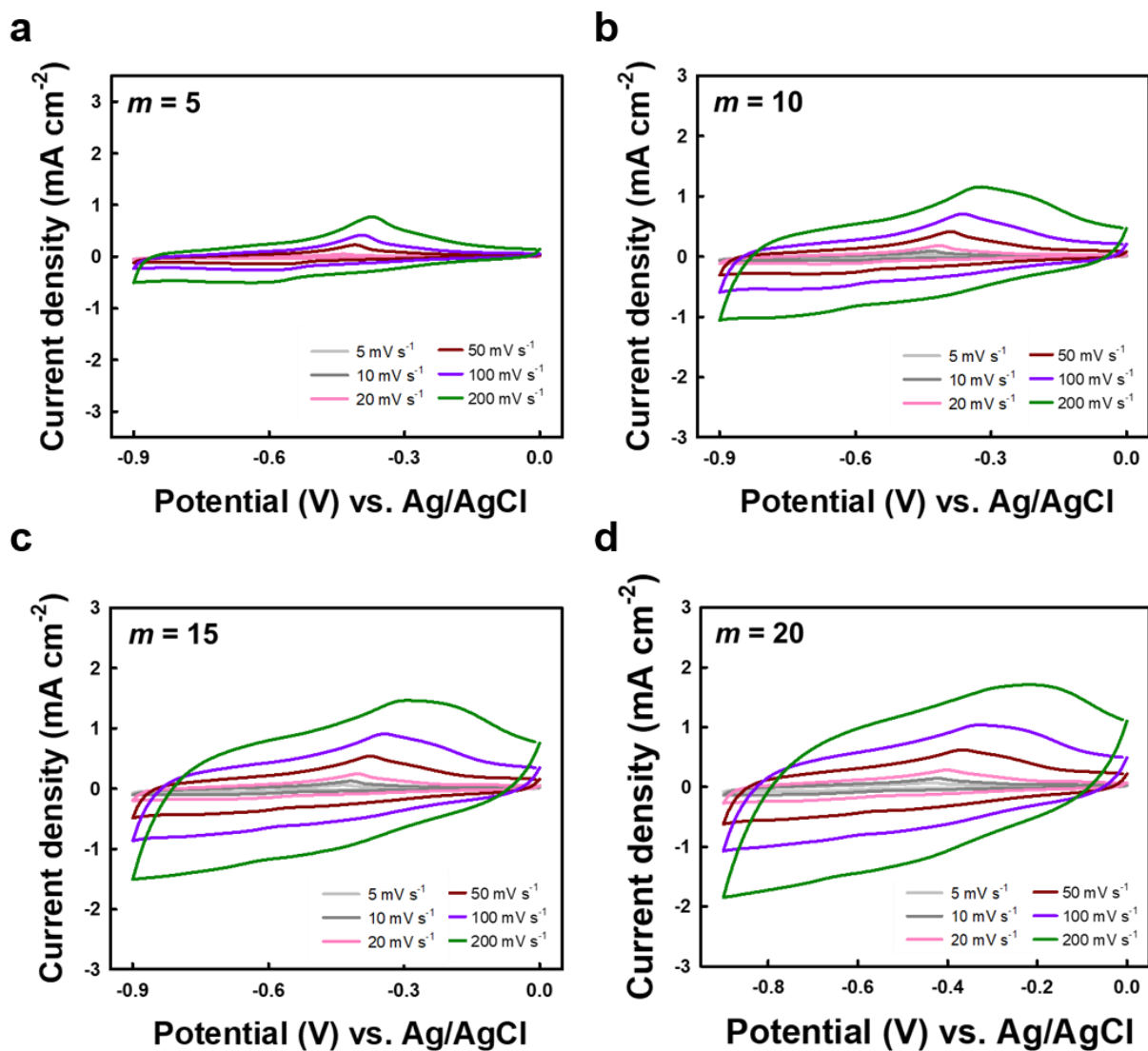
Fig. S18. CV curves for periodic number-dependent (Fe₃O₄ NP/MnPP/ITO NP/MnPP)$_m$ electrodes at different scan rates ranging from 5 to 200 mV s^{-1}: (a) m = 5, (b) m = 10, (c) m = 15, and (d) m = 20.
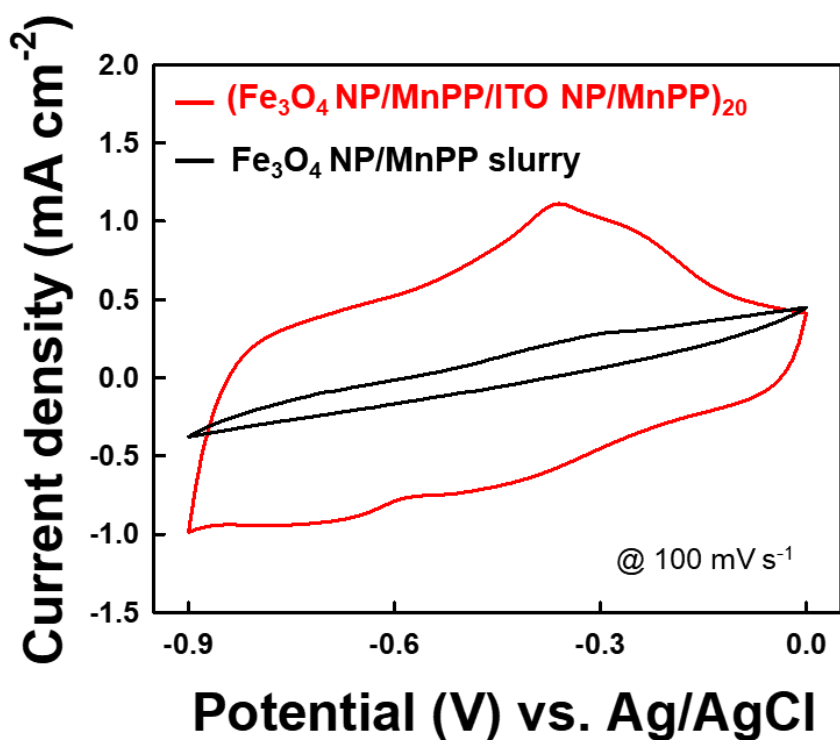
Fig. S19. Compariosn of CV curves between (Fe₃O₄ NP/MnPP/ITO NP/MnPP)₂₀ electrode and slurry-cast electrode at a scan rate of 100 mV s⁻¹. In this case, the active slurry was prepared by physical mixing of active materials (i.e., Fe_3O_4 NP and MnPP), carbon black, and PAA with a mass ratio of 8:1:1, and the mass loading of active materials was adjusted equal with that of (Fe₃O₄ NP/MnPP/ITO NP/MnPP)₂₀ electrode.
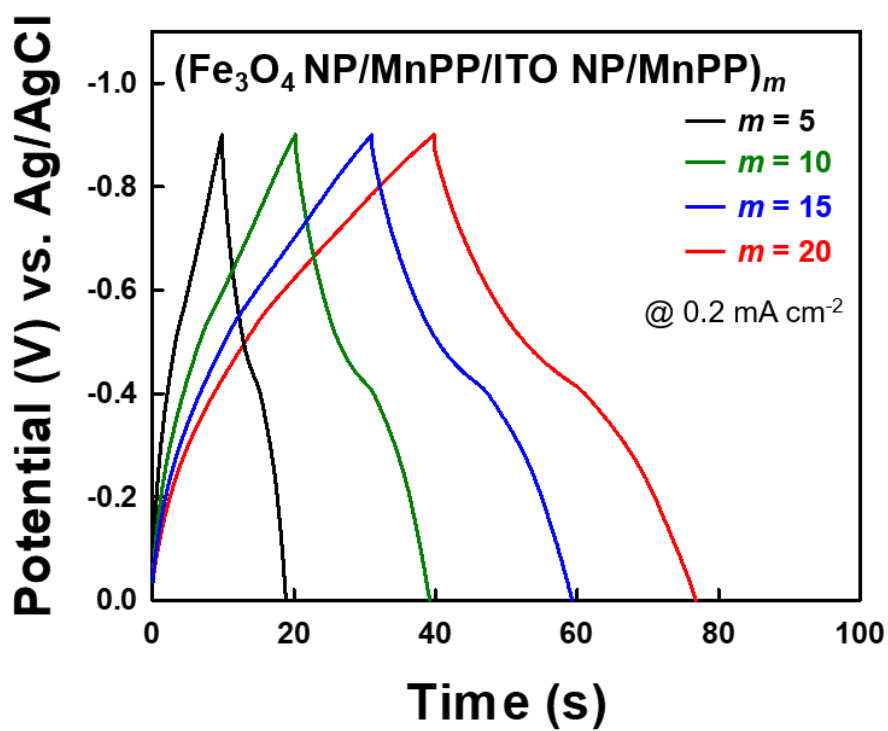
Fig. S20. GCD curves of (Fe₃O₄ NP/MnPP/ITO NP/MnPP)$_m$ electrodes with different periodic numbers (m) at a current density of 0.2 mA cm^{-2}.
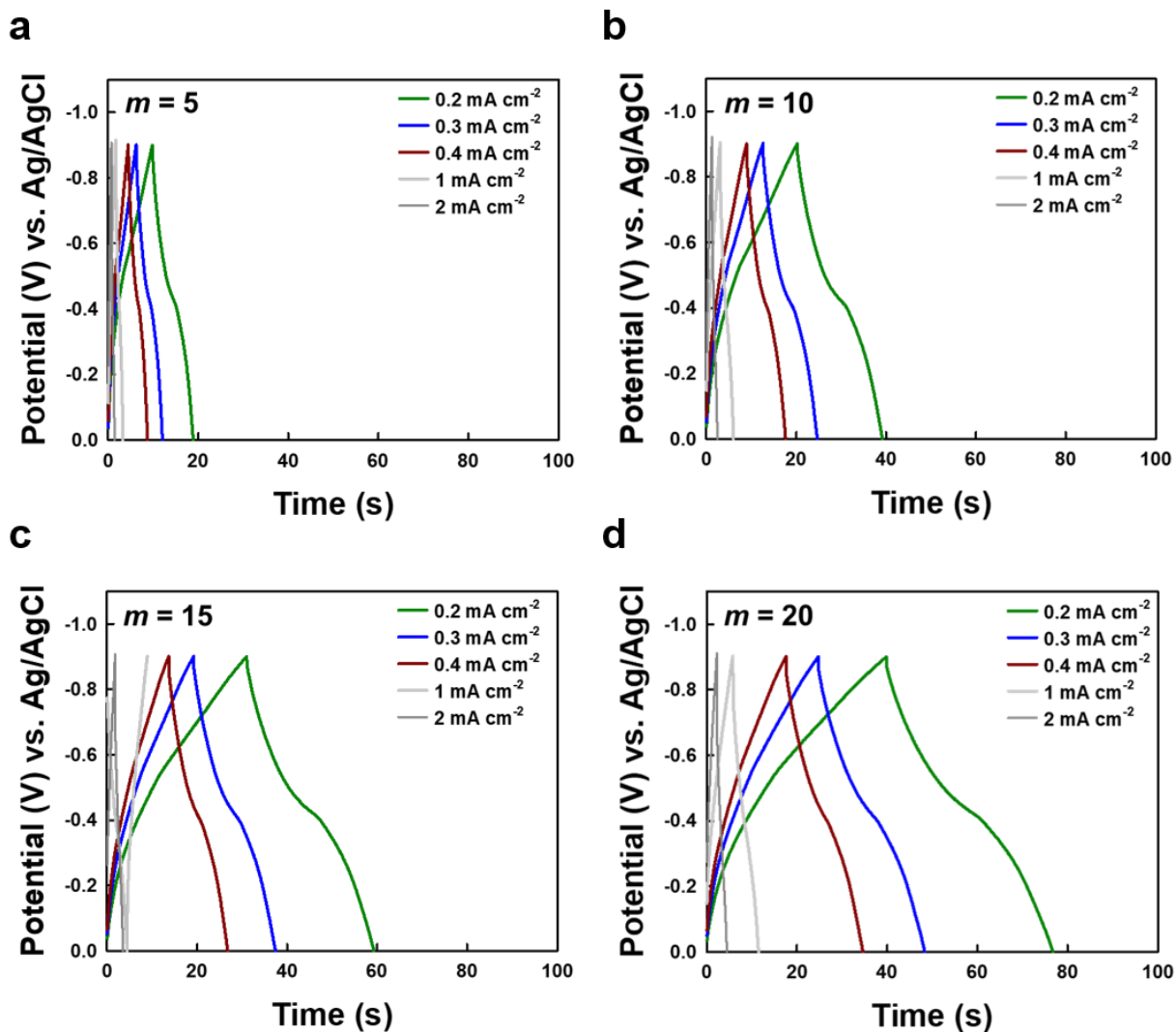
Fig. S21. GCD curves of (Fe$_3$O$_4$ NP/MnPP/ITO NP/MnPP)$_m$ electrodes with different periodic numbers (*m*) at various current densities ranging from 0.2 to 2.0 mA cm^{-2}: (a) *m* = 5, (b) *m* = 10, (c) *m* = 15, and (d) *m* = 20.
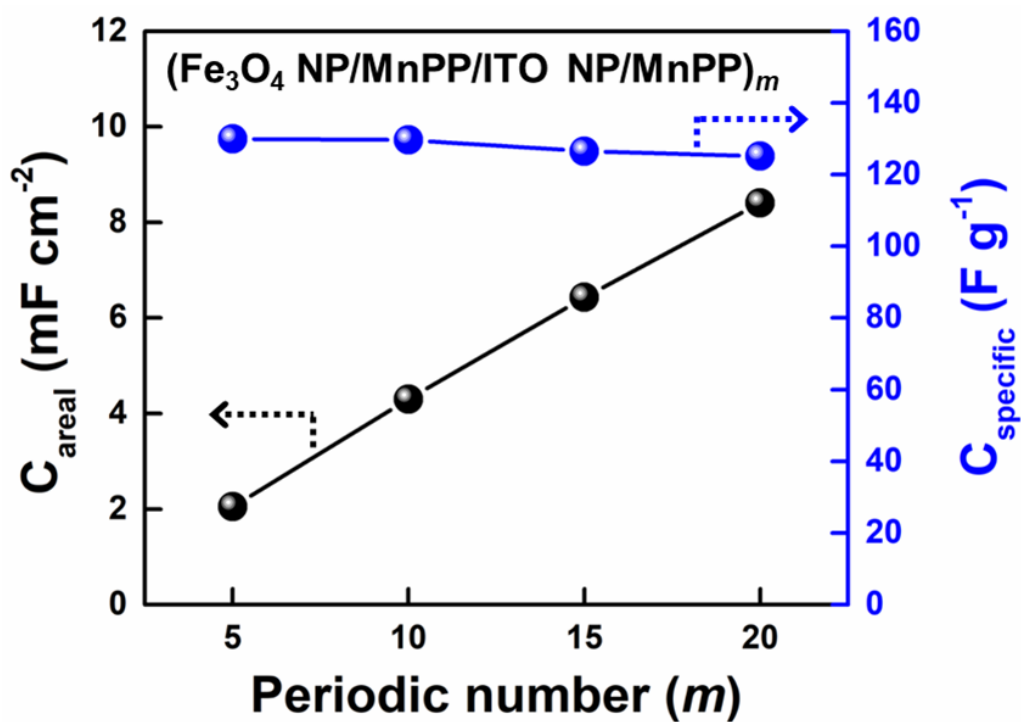
Fig. S22. Areal capacitance (C_{areal}, left axis) and specific capacitance ($C_{specific}$, right axis) of (Fe_3O_4 NP/MnPP/ITO NP/MnPP)$_m$ electrodes obtained from the GCD curves at a current density of 0.2 mA cm^{-2} as a function of periodic number (m).
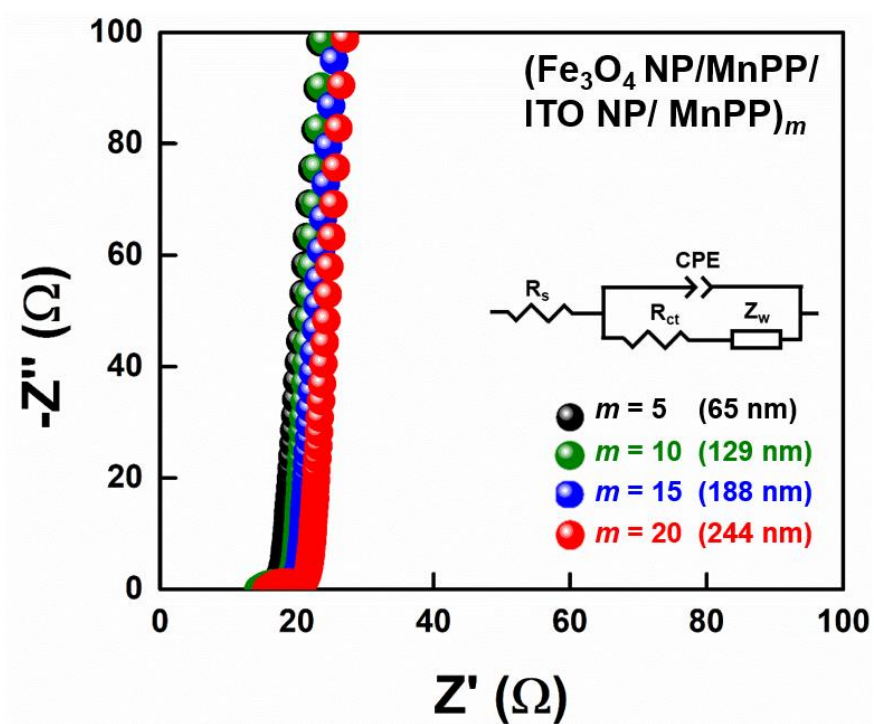
Fig. S23. Nyquist plots of (Fe$_3$O$_4$ NP/MnPP/ITO NP/MnPP)$_m$ electrodes with different periodic numbers (m) and their representative equivalent circuit (see the inset).
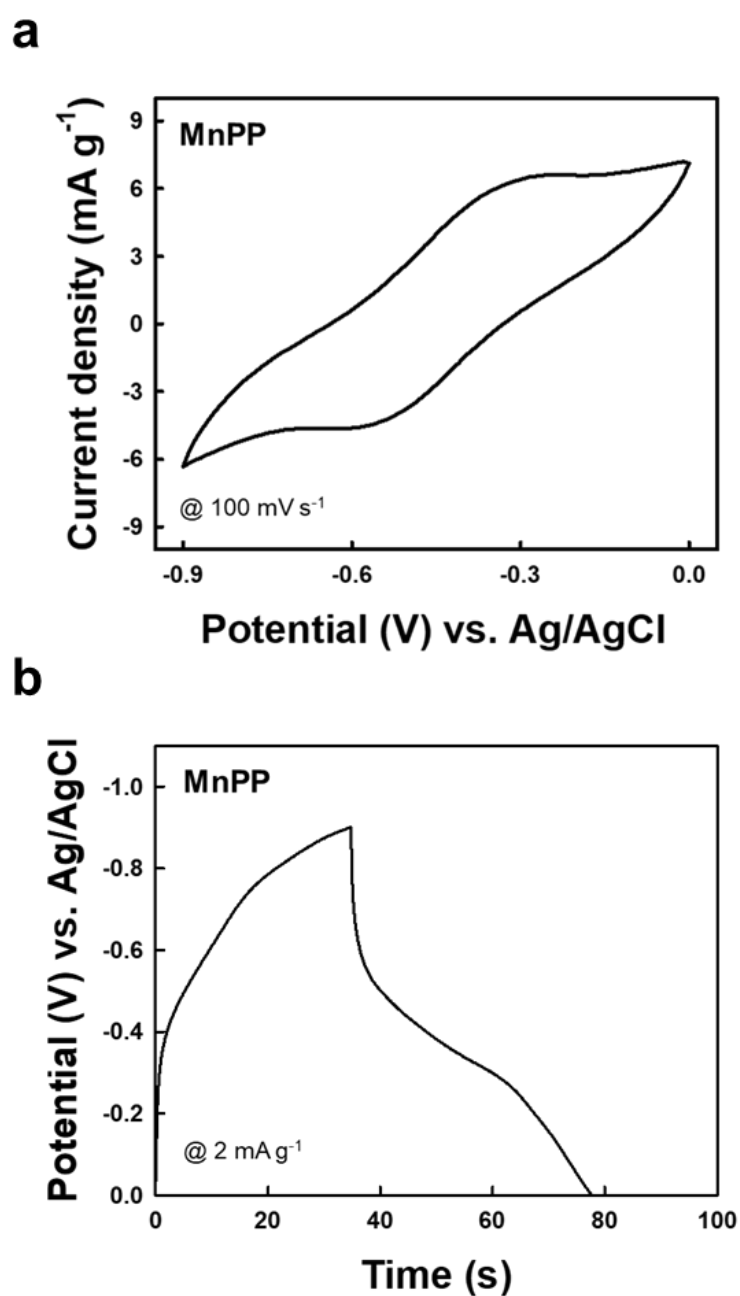
Fig. S24. (a) CV scan (at a scan rate of 100 mV s^{-1}) and (b) GCD curve (at a current density of 2.0 mA cm^{-2}) of MnPP electrode. The MnPP electrode was fabricated by conventional slurry casting composed of MnPP, carbon black, and PAA with a mass ratio of 5:5:1, followed by drying at 120 °C for 8 h. In this case, the experimental specific capacitance of MnPP was calculated to be ~98 F g^{-1} from the GCD curve.
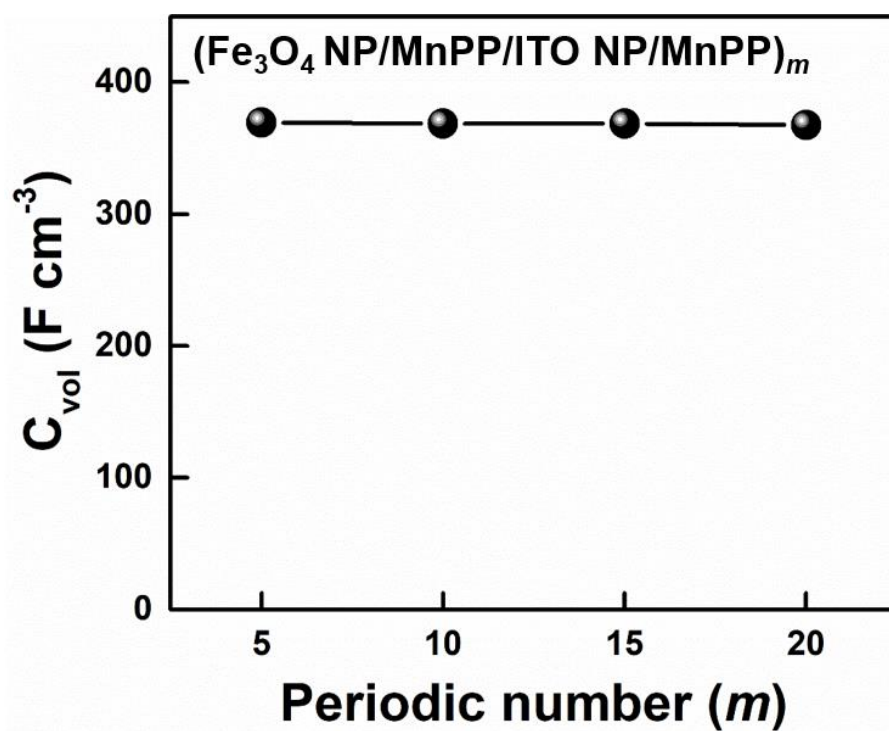
Fig. S25. Volumetric capacitance (C_{vol}) of (Fe$_3$O$_4$ NP/MnPP/ITO NP/MnPP)$_m$ electrodes measured from the GCD curves at a current density of 0.2 mA cm^{-2} as a function of periodic number (m).
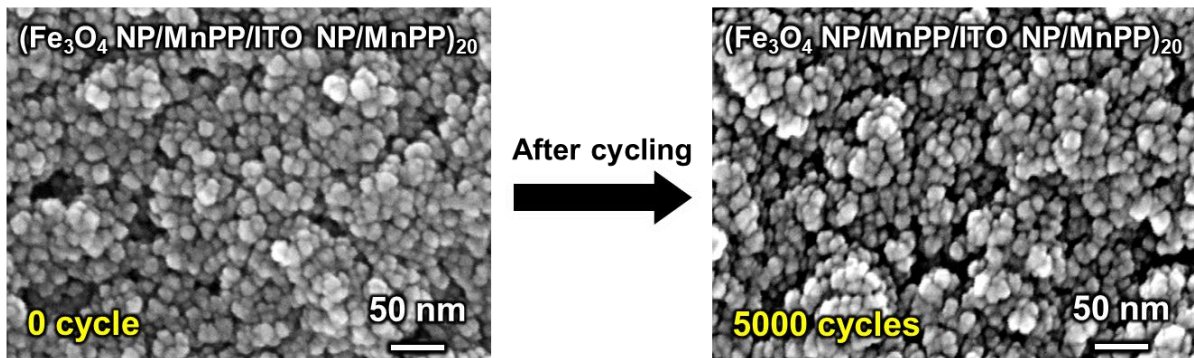
Fig. S26. Planar FE-SEM images of (Fe$_3$O$_4$ NP/MnPP/ITO NP/MnPP)$_{20}$ electrodes before and after 5000 GCD cycles at a current density of 0.5 mA cm^{-2}.
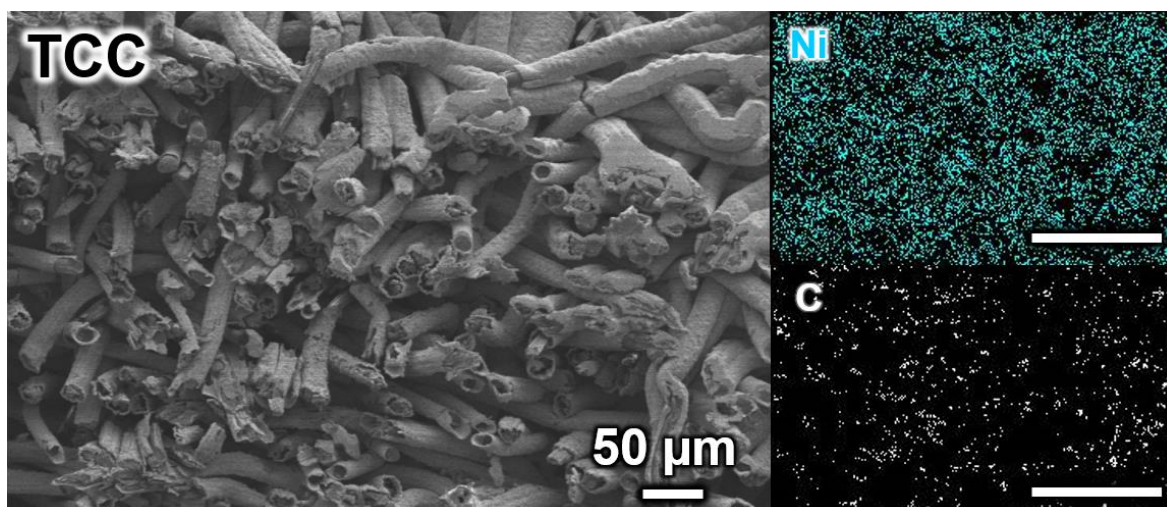
Fig. S27. Cross-sectional FE-SEM image and corresponding EDS mapping images of Ni electroplated textile, named as a textile-based current collector (TCC).
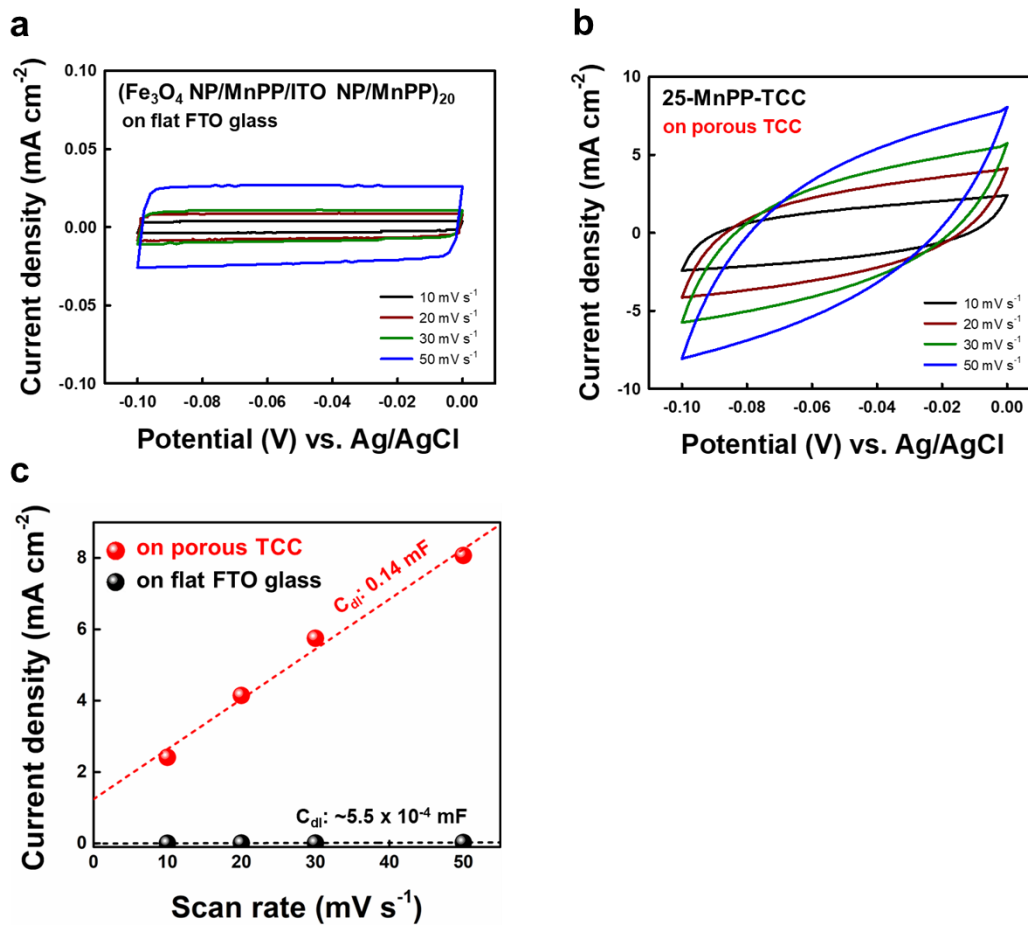
Fig. S28. Scan rate-dependent CV curves of (a) (Fe$_3$O$_4$ NP/MnPP/ITO NP/MnPP)$_{20}$ electrode and (b) 25-MnPP-TCC in the non-Faradaic potential region ranging from −0.1 to 0 V at different scan rates ranging from 10 to 50 mV s^{-1}. (c) Comparative plots of current *vs.* scan rate between (Fe$_3$O$_4$ NP/MnPP/ITO NP/MnPP)$_{20}$ electrode and 25-MnPP-TCC. In this case, the double-layer capacitances (C$_{dl}$) were obtained from the linearly fitted slopes.
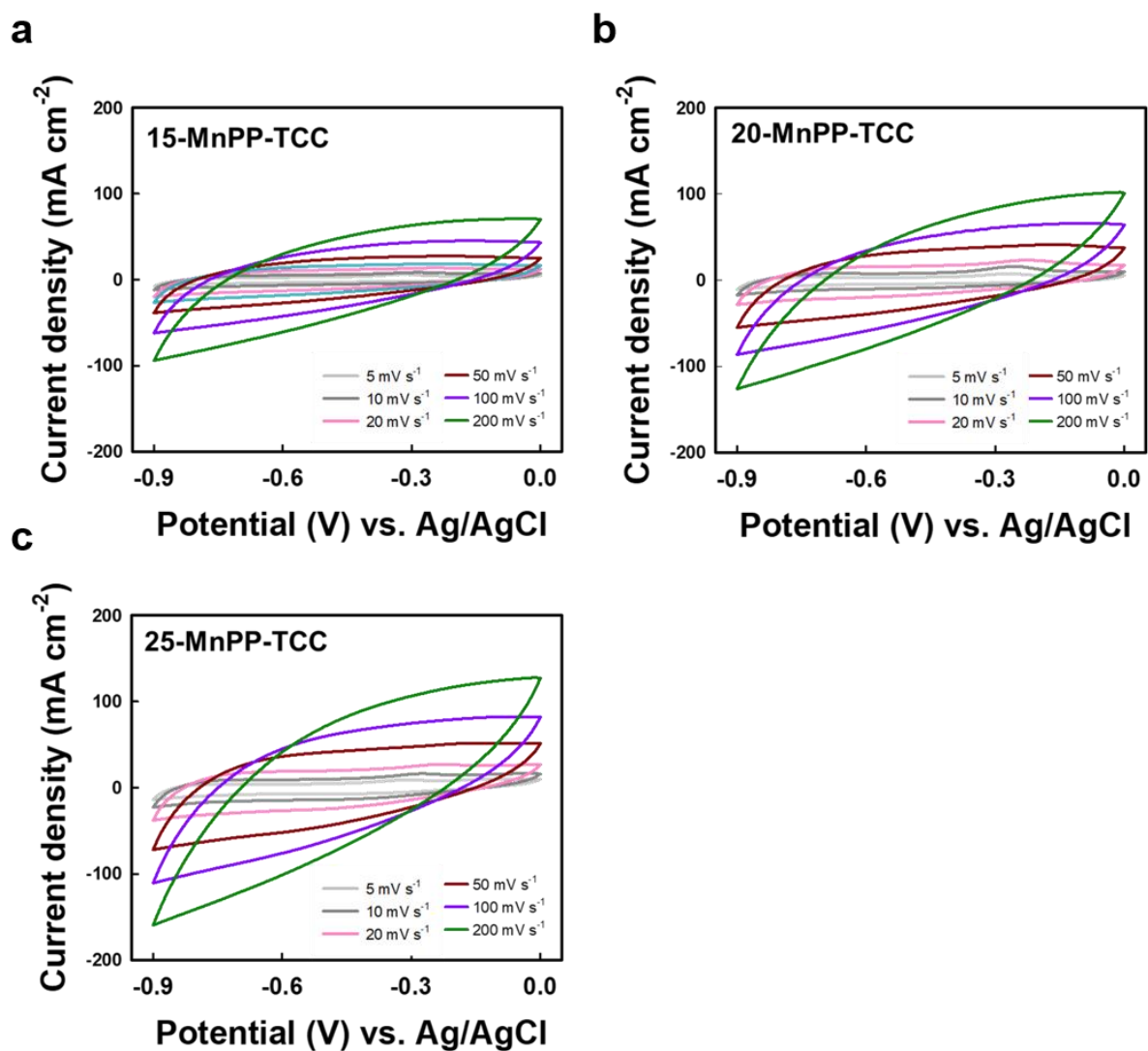
Fig. S29. CV curves of *m*-MnPP-TCCs at different scan rates ranging from 5 to 200 mV s^{-1} for different periodic numbers (*m*): (a) *m* = 15, (b) *m* = 20, and (c) *m* = 25.
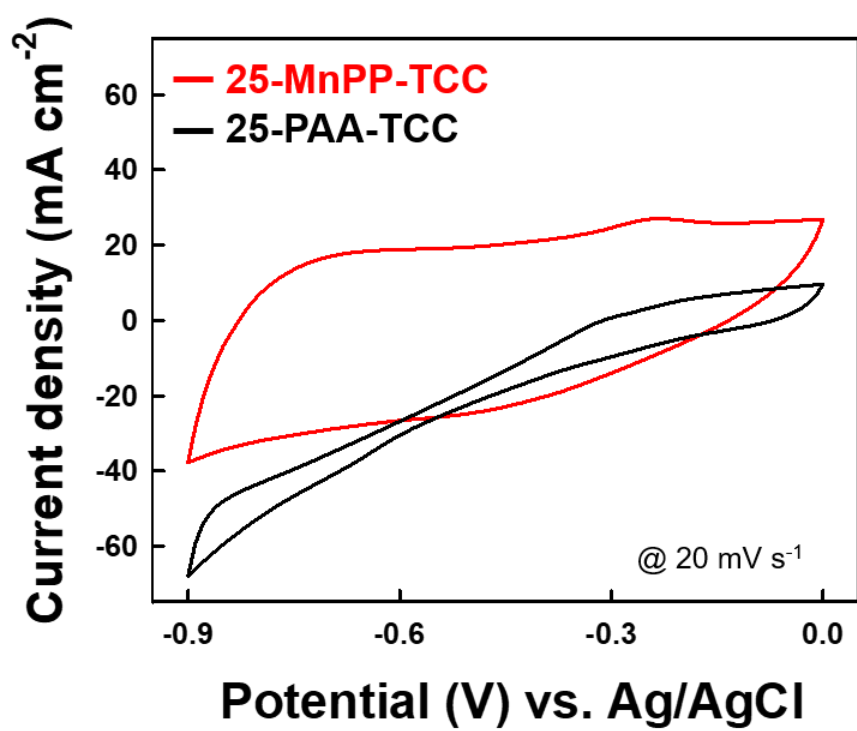
Fig. S30. CV curves of 25-MnPP-TCC and 25-PAA-TCC at a scan rate of 20 mV s^{-1}.
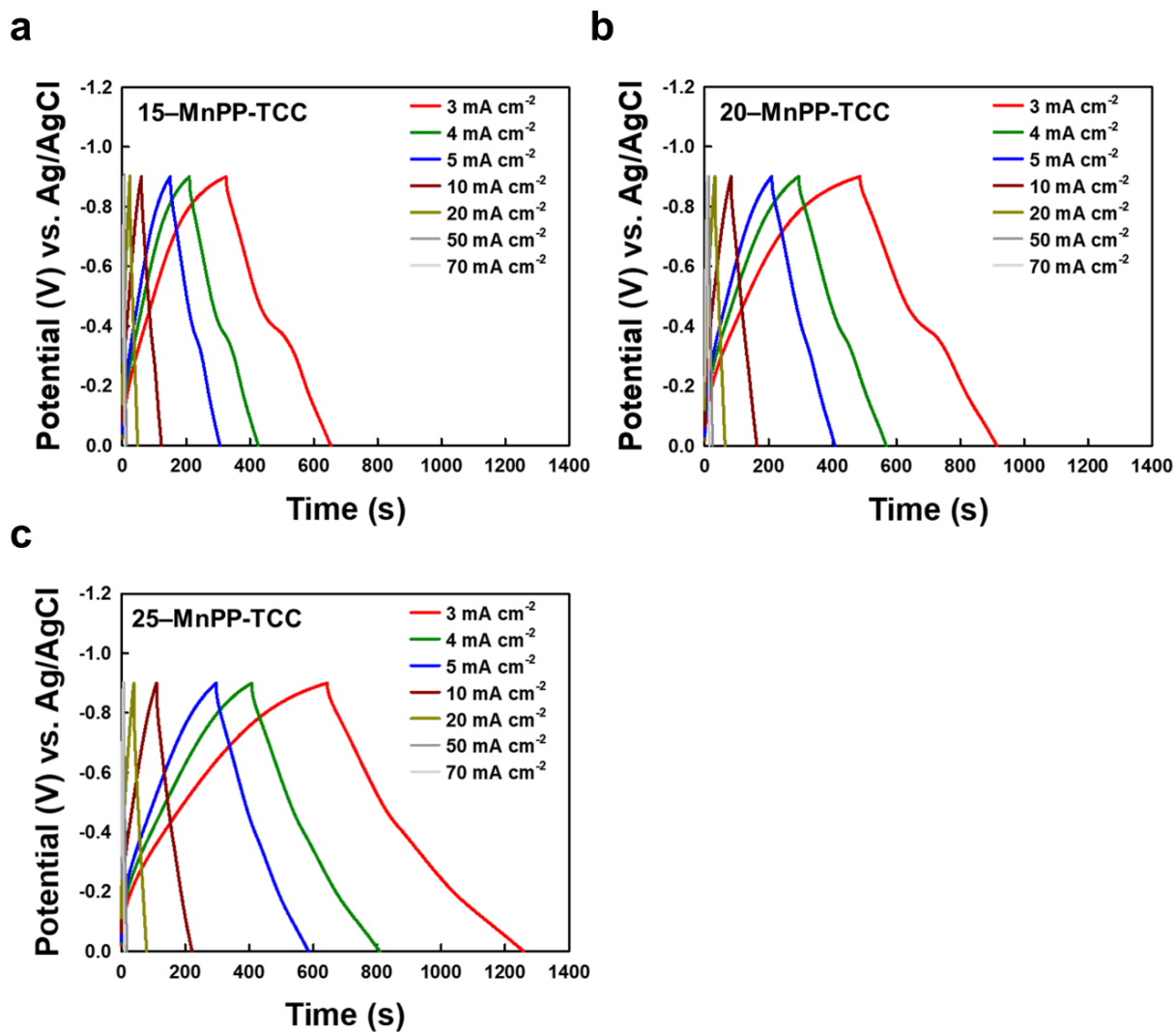
Fig. S31. GCD curves of *m*-MnPP-TCCs at different current densities ranging from 3.0 to 70 mA cm^{-2} for different periodic numbers (*m*): (a) *m* = 15, (b) *m* = 20, and (c) *m* = 25.
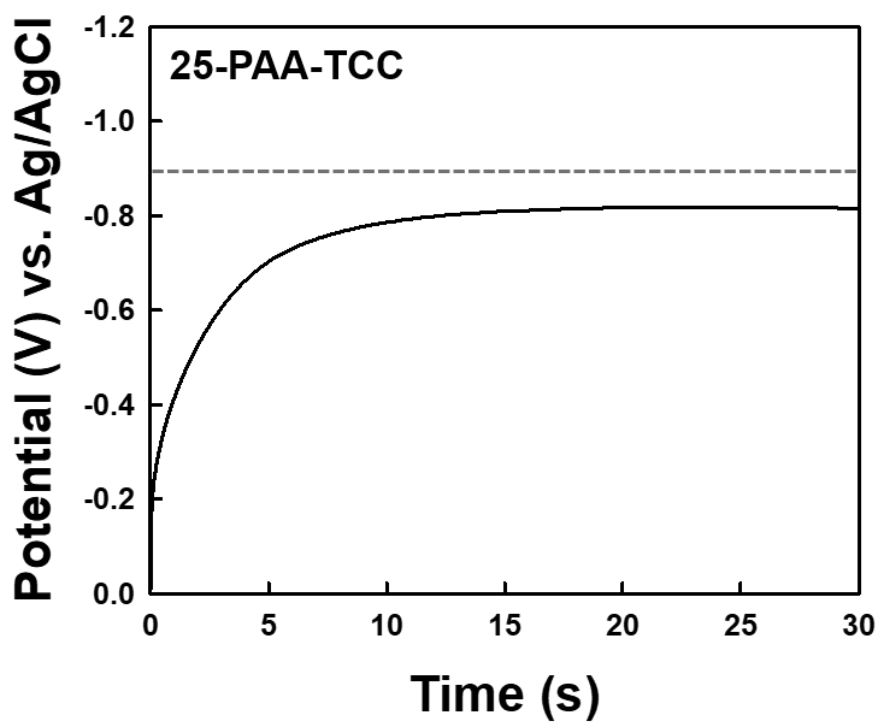
Fig. S32. GCD curve of 25-PAA-TCC in a charging step at a current density of 30 mA cm^{-2}.
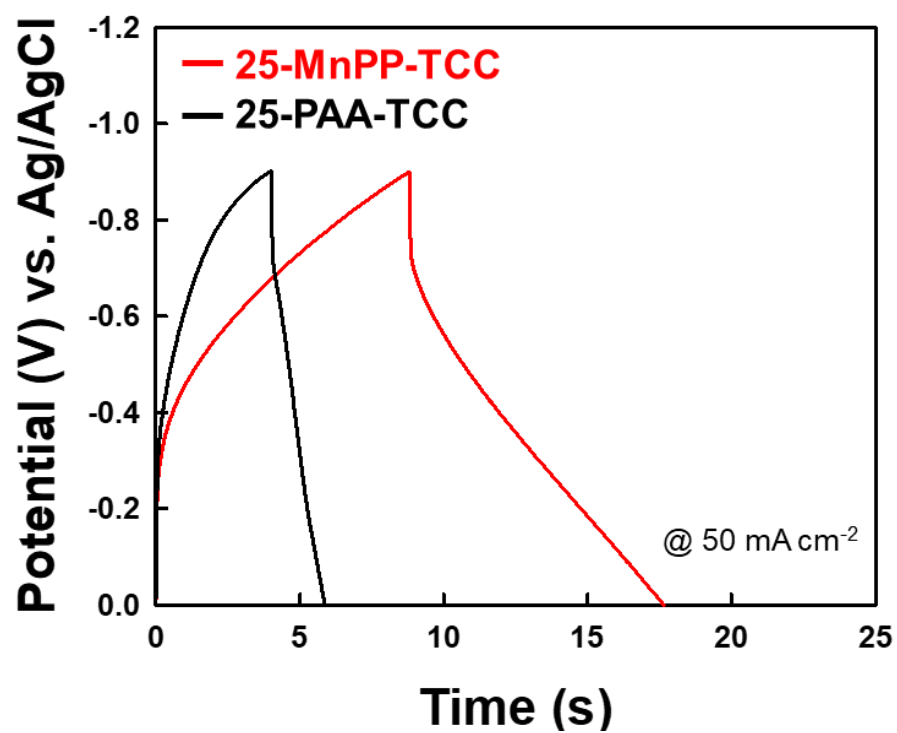
Fig. S33. GCD curves of 25-MnPP-TCC and 25-PAA-TCC electrodes at a current density of 50 mA cm^{-2}.
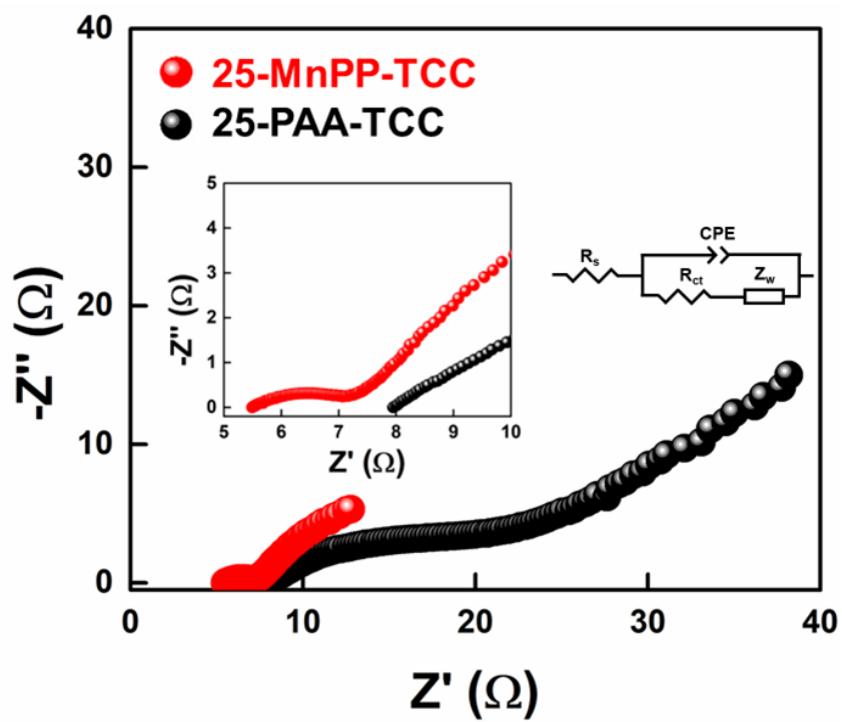
Fig. S34. Nyquist plots with a representative equivalent circut (the inset) of 25-MnPP-TCC and 25-PAA-TCC.
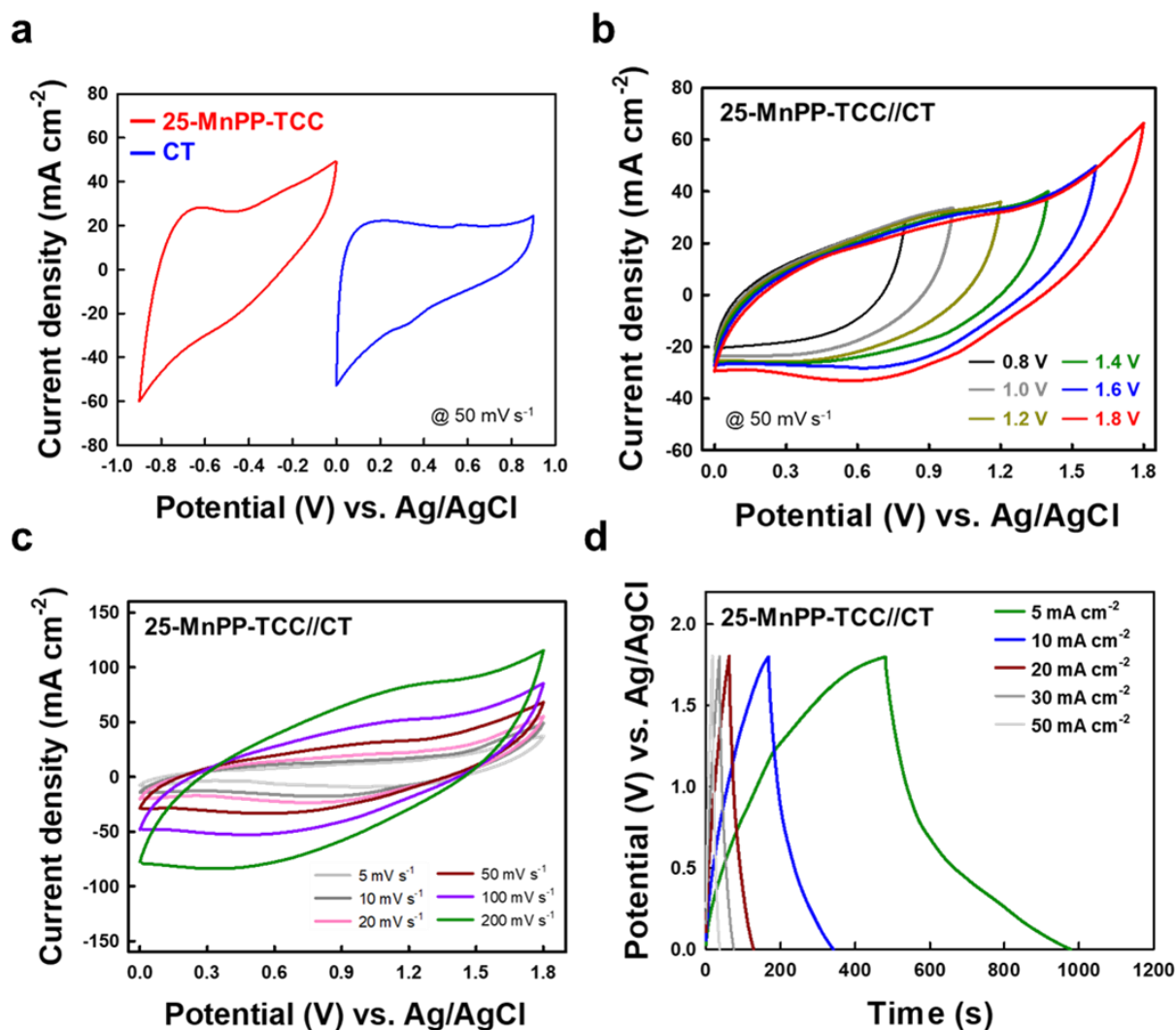
Fig. S35. Electrochemical performance of 25-MnPP-TCC//CT. (a) CV curves of negative 25-MnPP-TCC electrode and positive CT electrode in a potential window ranging from −0.9 to 0 V and from 0 to 0.9 V (*vs.* Ag/AgCl), respectively. (b) CV curves of 25-MnPP-TCC//CT with increasing the potential window from 0.8 to 1.8 V. (c) Scan rate-dependent CV curves and (d) current density-dependent GCD curves of 25-MnPP-TCC//CT.

Table S1. Comparison of areal capacitances of Fe_3O_4-based electrodes.

| Electrode materials	Electrolyte	Mass density (mg cm^{-2})	Areal capacitance (mF cm^{-2})	Current density /Scan rate	Ref.
25-TCC-MnPP	**1.0 M Na$_2$SO$_3$**	**3.9**	**2100**	**3.0 mA cm^{-2}**	**Our work**
Fe_3O_4/PANI nanonets	1.0 M H$_2$SO$_4$	2.0	1240	2.0 mA cm^{-2}	[S8]
Fe_3O_4/carbon	3.0 M KOH	1.5	804	4.5 mA cm^{-2}	[S9]
Fe_3O_4/FeOOH nanowire	0.5 M Na$_2$SO$_3$	1.5	468	2.0 mV s^{-1}	[S10]
Fe_3O_4 [a)]NA @2D-[b)]CCS	6.0 M KOH	1.5~2.0	1435	1.0 mA cm^{-2}	[S11]
Fe_3O_4–CNT	1.0 M Na$_2$SO$_4$	3.0	1165	10 mV s^{-1}	[S12]
[c)]CNF/[d)]CNS /Fe$_3$C@Fe$_3$O$_4$	1.0 M KOH	1.3~1.5	491	7.5 mA cm^{-2}	[S13]
Fe_3O_4/[c)]CNF	3.0 M KOH	1.2~1.5	338	1.5 mA cm^{-2}	[S14]
Fe_3O_4@Fe$_2$O$_3$	1.0 M Na$_2$SO$_4$	1.3	1447	5.0 mV s^{-1}	[S15]
Fe_3O_4@[e)]CNB	6.0 M KOH	2.0	932	0.4 mA cm^{-2}	[S16]
Fe_2O_3/RGO /Fe$_3$O$_4$	2.0 M KOH	4.3	337	20 mV s^{-1}	[S17]
Fe_3O_4 NP/PANI	1.0 M H$_2$SO$_4$	2.0	1144	2.0 mA cm^{-2}	[S18]

[a)]NA: nano-assembly, [b)]CCS: crumpled porous carbon sheet, [c)]CNF: carbon nanofiber, [d)]CNS: carbon nanosheet, [e)]CNB: carbon nanocapsule.

*The areal capacitances were calculated from the given data in the literature.

Table S2. Comparison of areal energy/power densities of assymmetric pseudocapacitors using Fe_3O_4 as an active materials for negativie electrodes.

Electrode materials	Electrolyte	Mass density $(mg\ cm^{-2})$	Areal Energy density $(\mu W\ h\ cm^{-2})$	Areal Power density $(mW\ cm^{-2})$	Ref.
25-TCC-MnPP//CT	**1.0 M Na_2SO_4**	**3.9**	**613**	**39.5**	**Our work**
$CNT–Fe_3O_4//CNT–Mn_3O_4$	1.0 M Na_2SO_4	2.0	68.2	20.6	[S19]
$Fe_3O_4@C//Na0.5MnO_2$	1.0 M Na_2SO_4	~1.5	121.5	30.0	[S20]
$Fe_2O_3/RGO/Fe_3O_4//Ni(OH)_2$	2.0 M KOH	2.1	8.6	13.9	[S21]
$C@Fe_3O_4//PEDOT@MnO_2$	1.0 M LiCl	2.7	33.5	0.6	[S22]
$FEG/Fe_3O_4-0.5//FEG/Ni-Co\ DH$	1.0 M KOH	1.0	54.0	17.0	[S23]
[a]$NCM-A600//CNTs$	3.0 M KOH	6.0	108.6	15.0	[S24]
$RGO@Fe_3O_4//CoO_x@Ni(OH)_2$	6.0 M KOH	2.6	118.2	18.5	[S25]
$Co−Fe_3O_4\ NS@NG//CoMnO_3@NG$	3.0 M KOH	3.0	267.3	54.1	[S26]

[a]NCM-A600: Fe_3O_4 NP electrode imbeded in nanostructured carbon materials at 600°C.

Supplementary references

[S1] S. J. Lee, C. D. Malliakas, M. G. Kanatzidis, J. T. Hupp, S. T. Nguyen, Amphiphilic porphyrin nanocrystals: Morphology tuning and hierarchical assembly, Adv. Mater. 5 (2008) 3543-3549, https://doi.org/10.1002/adma.200800003.

[S2] S. Sun, H. Zeng, D. B. Robinson, S. Raoux, P. M. Rice, S. X. Wang, G. Li, Monodisperse MFe_2O_4 (M = Fe, Co, Mn) nanoparticles, J. Am. Chem. Soc. 126 (2004) 273-279, https://doi.org/10.1021/ja0380852.

[S3] M. Kanehara, H. Koike, T. Yoshinaga, T. Teranishi, Indium tin oxide nanoparticles with compositionally tunable surface plasmon resonance frequencies in the near-IR region, J. Am. Chem. Soc. 131 (2009) 17736-17737, https://doi.org/10.1021/ja9064415.

[S4] S. Woo, D. Nam, W. Chang, Y. Ko, S. Lee, Y. Song, B. Yeom, J. H. Moon, S. W. Lee, J. Cho, A Layer-by-layer assembly route to electroplated fibril-based 3D porous current collectors for energy storage devices, Small 17 (2021) 2007579, https://doi.org/10.1002/smll.202007579.

[S5] M. R. Deakin, D. A. Buttry, Electrochemical applications of the quartx crystal microbalance, Anal. Chem. Soc. 61 (1989) 1147A-1154A.

[S6] L. J. Boucher, J. J. Katz, The infrared spectra of metalloporphyrins (4000-160 cm^{-1}), J. Am. Chem. Soc. 89 (1966) 1340-1345, https://doi.org/10.1021/ja00982a011.

[S7] A. G. Zelinsky, B. Y. Pirogov, Electrochemical oxidation of sulfite and sulfur dioxide at a renewable graphite electrode, Electrochim. Acta 231 (2017) 371-378, https://doi.org/10.1016/j.electacta.2017.02.070.

[S8] Y. Ma, C. Hou, H. Zhanb, Q. Zhang, H. Liu, S. Wu, Z. Guo, Three-dimensional core-shell Fe3O4/polyaniline coaxial heterogeneous nanonets: preparation and high performance supercapacitor electrodes, Electrochim. Acta 315 (2019) 114-123, https://doi.org/10.1016/j.electacta.2019.05.073.

[S9]   S. Kaipannan, K. Govindarajan, S. Sundaramoorthy, S. Marappan, Waste toner-derived carbon/Fe3O4 nanocomposite for high-performance supercapacitor, ACS Omega 4 (2019) 15798-15805, https://doi.org/10.1021/acsomega.9b01337.

[S10]   L. O'Neill, C. Johnston, P. S. Grant, Enhancing the supercapacitor behaviour of novel Fe_3O_4/FeOOH nanowire hybrid electrodes in aqueous electrolytes, J. Power Sources 274 (2015) 907-915, http://dx.doi.org/10.1016/j.jpowsour.2014.09.151.

[S11]   S. Venkateswarlu, H. Mahajan, A. Panda, J. Lee, S. Govindaraju, K. Yun, M. Yoon, Fe_3O_4 nano assembly embedded in 2D-crumpled porous carbon sheets for high energy density supercapacitor, Chem. Eng. J. 420 (2021) 127584, https://doi.org/10.1016/j.cej.2020.127584.

[S12]   A. Kumar, D. Sarkar, S. Mukherjee, S. Patil, D. D. Sarma, A. Shukla, Realizing an asymmetric supercapacitor employing carbon nanotubes anchored to Mn_3O_4 cathode and Fe_3O_4 anode, ACS Appl. Mater. Interfaces 10 (2018) 42484-42493, https://doi.org/10.1021/acsami.8b16639.

[S13]   J. Ju, M. Kim, S. Jang, Y. Kim, Y. Choi, S-H. Baeck, S. E. Shim, 3D in-situ hollow carbon fiber/carbon nanosheet/$Fe_3C@Fe_3O_4$ by solventless one-step synthesis and its superior supercapacitor performance, Electrochim. Acta 252 (2017) 215-225, https://doi.org/10.1016/j.electacta.2017.09.002.

[S14]   C. Fu, A. Mahadevegowda, P. S. Grant, Fe_3O_4/carbon nanofibres with necklace architecture for enhanced electrochemical energy storage, J. Mater. Chem. A 3 (2015) 14245-14253, https://doi.org/10.1039/C5TA02210J.

[S15]   X. Tang, R. Jia, T. Zhai, H. Xia, Hierarchical $Fe_3O_4@Fe_2O_3$ core–shell nanorod arrays as high-performance anodes for asymmetric supercapacitors, ACS Appl. Mater. Interfaces 7 (2015) 27518-27525, https://doi.org/10.1021/acsami.5b09766.

[S16]   L. Wang, F. Liu, A. Pal, Y. Ning, Z. Wang, B. Zhao, R. Bradley, W. Wu, Ultra-small Fe3O4 nanoparticles encapsulated in hollow porous carbon nanocapsules for high

performance supercapacitors, Carbon 179 (2021) 327-336, https://doi.org/10.1016/j.carbon.2021.04.024.

[S17] C. Zhao, X. Shao, Y. Zhang, X. Qian, Fe_2O_3/reduced graphene oxide/Fe_3O_4 composite in situ grown on Fe foil for high-performance supercapacitors, ACS Appl. Mater. Interfaces 8 (2016) 30133-30142, https://doi.org/10.1021/acsami.6b09594.

[S18] T. Prasankumar, B. R. Wiston, C. R. Gautam, R. Ilangovan, S. P. Jose, Synthesis and enhanced electrochemical performance of PANI/Fe_3O_4 nanocomposite as supercapacitor electrode, J. Alloys Compd. 757 (2018) 466-475, https://doi.org/10.1016/j.jallcom.2018.05.108.

[S19] A. Kumar, D. Sarkar, S. Mukherjee, S. Patil, D. D. Sarma, A. Shukla, Realizing an asymmetric supercapacitor employing carbon nanotubes anchored to Mn_3O_4 cathode and Fe_3O_4 anode, ACS Appl. Mater. Interfaces 10 (2018) 42484-42493, https://doi.org/10.1021/acsami.8b16639.

[S20] N. Jabeen, A. Hussain, Q. Xia, S. Sun, J. Zhum, H. Xia, High-performance 2.6 V aqueous asymmetric supercapacitors based on in situ formed Na0.5MnO_2 nanosheet assembled nanowall arrays, Adv. Mater. 29 (2017) 1700804, https://doi.org/10.1002/adma.201700804.

[S21] C. Zhao, X. Shao, Y. Zhang, X. Qian, Fe_2O_3/reduced graphene oxide/Fe_3O_4 composite in situ grown on Fe foil for high-performance supercapacitors, ACS Appl. Mater. Interfaces 8 (2016) 30133-30142, https://doi.org/10.1021/acsami.6b09594.

[S22] J. Sun, Y. Huang, C. Fu, Y. Huang, M. Zhu, X. Tao, C. Zhi, H. Hu, A high performance fiber-shaped PEDOT@MnO_2//C@Fe_3O_4 asymmetric supercapacitor for wearable electronics. J. Mater. Chem. A 4 (2016) 14877-14883, https://doi.org/10.1039/C6TA05898A.

[S23] Z. Sun, X. Cai, Y. Song, X. Liu, Electrochemical deposition of honeycomb magnetite on partially exfoliated graphite as anode for capacitive applications, J. Power Sources 359 (2017) 57-63, https://doi.org/10.1016/j.jpowsour.2017.05.055.

[S24] L. Li, C. Jia, Z. Shao, J. Wang, F. Wang, W. Wang, H. Wang, D. Zu, H. Wu, Fe_3O_4/nitrogen-doped carbon electrodes from tailored thermal expansion toward flexible solid-state asymmetric supercapacitors, Adv. Mater. Interfaces 6 (2019) 1901250, https://doi.org/10.1002/admi.201901250.

[S25] J. Zhu, L. Huang, Y. Xiao, L. Shen, Q. Chen, W. Shi, Hydrogenated CoOx nanowire@Ni(OH)$_2$ nanosheet core–shell nanostructures for high-performance asymmetric supercapacitors, Nanoscale 6 (2014) 6772-6781, https://doi.org/10.1039/C4NR00771A.

[S26] M. Guo, J. Balamurugan, X. Li, N. H. Kim, J. H. Lee, Hierarchical 3D cobalt-doped Fe_3O_4 nanospheres@NG hybrid as an advanced anode material for high-performance asymmetric supercapacitors, Small 13 (2017) 1701275, https://doi.org/10.1002/smll.201701275.